



Published in final edited form as:

Cell Rep. 2019 February 05; 26(6): 1557–1572.e8. doi:10.1016/j.celrep.2019.01.057.

Respiratory Phenomics across Multiple Models of Protein Hyperacylation in Cardiac Mitochondria Reveals a Marginal Impact on Bioenergetics

Kelsey H. Fisher-Wellman^{1,8}, James A. Draper¹, Michael T. Davidson¹, Ashley S. Williams¹, Tara M. Narowski¹, Dorothy H. Slentz¹, Olga R. Ilkayeva¹, Robert D. Stevens¹, Gregory R. Wagner¹, Rami Najjar⁴, Mathew D. Hirschey^{1,2,5}, J. Will Thompson³, David P. Olson⁶, Daniel P. Kelly⁷, Timothy R. Koves¹, Paul A. Grimsrud^{1,*}, and Deborah M. Muoio^{1,2,5,9,*}

¹Duke Molecular Physiology Institute and Sarah W. Stedman Nutrition and Metabolism Center, Duke University Medical Center, Durham, NC 27701, USA

²Department of Pharmacology and Cancer Biology, Duke University Medical Center, Durham, NC 27710, USA

³Duke Proteomics and Metabolomics Shared Resource, Duke University Medical Center, Durham, NC 27710, USA

⁴Cell Signaling Technologies, Danvers, MA 01923, USA

⁵Department of Medicine, Division of Endocrinology, Metabolism, and Nutrition, Duke University Medical Center, Durham, NC 27710, USA

⁶Department of Pediatrics, Division of Pediatric Endocrinology, Michigan Medicine, Ann Arbor, MI 48109, USA

⁷Perelman School of Medicine, University of Pennsylvania, PA 19104, USA

⁸Present address: East Carolina Diabetes and Obesity Institute, Brody School of Medicine, Department of Physiology, East Carolina University, Greenville, NC 27834, USA

⁹Lead Contact

SUMMARY

Acyl CoA metabolites derived from the catabolism of carbon fuels can react with lysine residues of mitochondrial proteins, giving rise to a large family of post-translational modifications (PTMs).

This is an open access article under the CC BY-NC-ND license (<http://creativecommons.org/licenses/by-nc-nd/4.0/>).

*Correspondence: paul.grimsrud@duke.edu (P.A.G.), muoio@duke.edu (D.M.M.).

AUTHOR CONTRIBUTIONS

Conceptualization, K.H.F.-W., D.P.K., T.R.K., P.A.G., and D.M.M.; Methodology, K.H.F.-W., P.A.G., T.R.K., and D.M.M.; Software, J.A.D.; Investigation, K.H.F.-W., M.T.D., A.S.W., J.A.D., P.A.G., J.W.T., D.H.S., R.D.S., O.R.I., G.R.W., T.M.N., and M.D.H.; Writing – Original Draft, K.H.F.-W., P.A.G., and D.M.M.; Writing – Review & Editing, K.H.F.-W., M.T.D., M.D.H., J.W.T., D.P.O., D.P.K., T.R.K., and D.M.M.; Funding Acquisition, P.A.G., A.S.W., K.H.F.-W., D.P.K., and D.M.M.

SUPPLEMENTAL INFORMATION

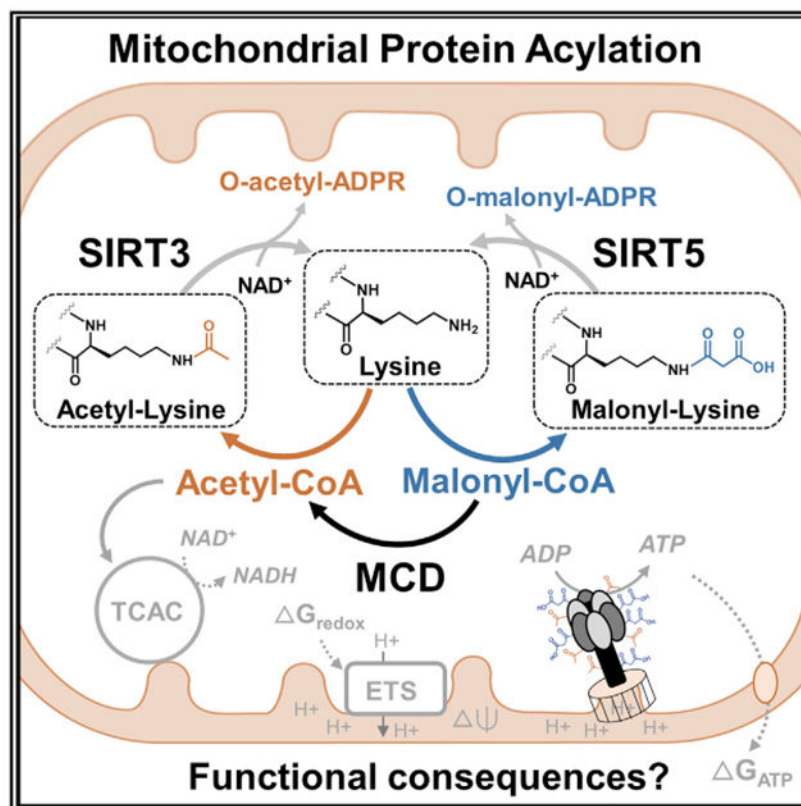
Supplemental Information includes eight figures and two tables and can be found with this article online at <https://doi.org/10.1016/j.celrep.2019.01.057>.

DECLARATION OF INTERESTS

The authors declare no competing interests.

Mass spectrometry-based detection of thousands of acyl-PTMs scattered throughout the proteome has established a strong link between mitochondrial hyperacylation and cardiometabolic diseases; however, the functional consequences of these modifications remain uncertain. Here, we use a comprehensive respiratory diagnostics platform to evaluate three disparate models of mitochondrial hyperacylation in the mouse heart caused by genetic deletion of malonyl CoA decarboxylase (MCD), SIRT5 demalonylase and desuccinylase, or SIRT3 deacetylase. In each case, elevated acylation is accompanied by marginal respiratory phenotypes. Of the >60 mitochondrial energy fluxes evaluated, the only outcome consistently observed across models is a ~15% decrease in ATP synthase activity. In sum, the findings suggest that the vast majority of mitochondrial acyl PTMs occur as stochastic events that minimally affect mitochondrial bioenergetics.

Graphical Abstract



In Brief

Fisher-Wellman et al. use a recently developed mitochondrial diagnostics platform for deep phenotyping of heart mitochondria derived from three disparate genetic models of protein hyperacylation. Their findings oppose the notion that hyperacylation of the mitochondrial proteome leads to broad-ranging vulnerabilities in respiratory function and bioenergetics.

INTRODUCTION

Acyl coenzyme A (CoA) molecules, which hold a prominent position in mitochondrial metabolism as intermediates of fuel oxidation, fluctuate in response to energy supply and demand. Accumulation of acyl CoAs within the mitochondrial matrix gives rise to increased production of their cognate acyl-carnitine conjugates through the action of carnitine acyltransferase enzymes. Numerous studies have identified elevated tissue and plasma levels of acyl CoAs and/or acylcarnitines in the context of a wide variety of metabolic disorders, including obesity, diabetes, and heart failure, and inborn errors of metabolism (McCoin et al., 2015; Newgard, 2017). Because acyl CoAs are reactive and potentially toxic at high levels (Wagner and Hirschey, 2014; Wagner et al., 2017), this class of metabolites has been directly implicated in carbon-induced mitochondrial stress. One theory gaining strong traction suggests acyl CoA molecules disrupt mitochondrial function by serving as substrates for non-enzymatic acylation of proteins on the epsilon amino group of lysine residues (Weinert et al., 2013a, 2013b, 2014, 2015). This family of posttranslational modifications (PTMs) are prominently found on mitochondrial proteins (Kim et al., 2006), which are presumably more vulnerable to acylation because of the high acyl CoA content and slightly basic pH of the matrix (Davies et al., 2016a; Koves et al., 2008; Paik et al., 1970; Poburko et al., 2011; Wagner and Payne, 2013). Accordingly, the detectable mitochondrial lysine acylome increases in the context of numerous metabolic diseases, including heart failure (Davies et al., 2016a; Du et al., 2015; Horton et al., 2016; Pougovkina et al., 2014). These observations have led to the prevailing view that lysine acylation serves as a common mechanism by which carbon surplus disrupts protein function and/or quality, thereby compromising metabolic and respiratory reserve in a manner that increases organ susceptibility to energetic stress (Baeza et al., 2016). The best evidence to support this theory comes from studies in mice lacking one or more of the mitochondrial sirtuins, a family of NAD⁺-dependent deacylases that includes SIRT3, the major mitochondrial deacetylase, and SIRT5, which acts as both a demalonylase and a desuccinylase. Although mice with deficiency of either SIRT3 or SIRT5 have modest phenotypes under basal conditions (Fernandez-Marcos et al., 2012; Yu et al., 2013), they show increased susceptibility to metabolic insults, supporting a link between protein deacylation and stress resistance (Hebert et al., 2013; Hershberger et al., 2017; Lantier et al., 2015; Sadhukhan et al., 2016). Whereas these reports provide a conceptually satisfying model of nutrient-induced mitochondrial stress, direct evidence that protein acylation does indeed impose wide-ranging bioenergetic vulnerabilities remains sparse.

The current study sought to test the hypothesis that broad-ranging lysine hyperacylation of metabolic proteins leads to latent vulnerabilities in mitochondrial function and bioenergetics. To this end, we leveraged a recently developed mitochondrial diagnostics platform to comprehensively evaluate respiratory fluxes and energy transfer in mitochondria harvested from cardiac tissues with high relative levels of protein acylation due to genetically engineered enzyme deficiencies. Mice with heart- and muscle-specific malonyl CoA decarboxylase (MCD) deficiency were used to model inborn errors in metabolism that result in lysine acylation due to acyl CoA accumulation. MCD is predominately localized to the mitochondrial matrix, where it degrades malonyl-CoA to acetyl CoA. In humans with loss-

of-function genetic mutations in the *MLYCD* gene, MCD enzyme inactivity results in marked accumulation of malonyl CoA and malonylcarnitine (Colak et al., 2015; Pougovkina et al., 2014). Malonyl CoA is a particularly relevant molecule, because it is nutritionally regulated and more reactive than acetyl CoA (Kulkarni et al., 2017), thus malonylation of mitochondrial proteins might underlie respiratory defects that contribute to cardiomyopathy in humans affected by MCD deficiency. Likewise, mice with transgenic knockout of *Sirt3* or *Sirt5* are predisposed to stress-induced heart failure, presumably due to PTMs that impede mitochondrial function (Hershberger et al., 2017; Horton et al., 2016; Koentges et al., 2015). We therefore enlisted these two additional mouse lines as models of hyperacylation resulting from deacylase inactivity. Despite widespread hyperacylation of the mitochondrial proteome in all three models, the bioenergetic phenotypes observed in isolated mitochondria were inconsistent with broad-ranging respiratory insufficiencies.

RESULTS

Loss of MCD Increases Malonyl-CoA and Drives Lysine Malonylation

Deficiency of MCD promotes lysine malonylation (*Kmal*) in human fibroblasts (Colak et al., 2015). To investigate whether a similar phenomenon occurs in the heart, we bred mice harboring floxed alleles of the *Mlycd* gene ($MCD^{fl/fl}$) with MCK-Cre transgenic mice to generate a muscle specific model of MCD deficiency ($MCD^{M-/-}$) (Figure S1). Heart and skeletal muscle tissues from these mice were interrogated using flow injection tandem mass spectrometry (MS/MS)-based metabolic profiling. As anticipated, these assays revealed elevations in the isobaric peaks corresponding to malonyl/hydroxyisovaleryl-carnitine (Figure 1A; indicated in red; Figures S2A and S2B) and malonyl/hydroxybutyryl-CoA (Figure 1A; indicated in blue; Figures S2C and S2D), but little or no changes in other metabolites. Subsequent analyses via liquid chromatography-tandem mass spectrometry (LC-MS/MS) confirmed the identities of the metabolites accumulating in the MCD-deficient tissues as malonyl-CoA (Figure 1B) and malonyl-carnitine (Figure 1C), the latter of which is likely produced within the mitochondrial matrix. Consistent with these observations, subcellular fractionation experiments revealed that MCD is enriched in mitochondria (Figure 1D). Elevated levels of malonyl CoA were accompanied by clear elevations in *Kmal*, detected by immunoblot analyses performed with an anti-malonyl-lysine antibody (Cell Signaling; 14942S). These PTMs appeared to be enriched in the mitochondrial compartment, relative to the whole-cell lysate (Figure S2H). Protein expression of the SIRT5 demalonylase and desuccinylase was unaffected by genotype (Figure S3C). Immunoblot analysis of *Kmal* in liver and brain lysates from $MCD^{fl/fl}$ or $MCD^{M-/-}$ mice (Figure S3D) was also negative.

Whereas elevations in cytosolic malonyl CoA might be expected to oppose fatty acid oxidation by inhibiting carnitine palmitoyltransferase I (CPT1) (McGarry et al., 1978), thereby lowering tissue levels of its long chain acylcarnitine products, we found little evidence for this effect (Figures S2A and S2B). Likewise, the whole-body metabolic phenotype of the mice was unremarkable (Figures S3A and S3B). These findings are consistent with previous studies in total body MCD knockout (KO) mice, which showed little impact of the deficiency when animals were fed *ad libitum* on a low-fat, standard chow

diet (Koves et al., 2008; Ussher et al., 2016). In light of this modest whole-body metabolic phenotype, the model was considered well suited for studies aimed at investigating the specific role of malonylation in regulating mitochondrial bioenergetics.

Identification of Malonylated Lysine Residues by nLC-MS/MS

To characterize the specific proteins and residues affected by malonylation, we performed isobaric tag-assisted quantitative malonyl-proteomics analysis of whole-cell lysates from heart and skeletal muscle of $MCD^{fl/fl}$ and $MCD^{M-/-}$ mice according to the workflow detailed in Figure 1E and in the STAR Methods. Of the ~407 unique malonylated peptides identified across both skeletal muscle and heart at a 1% false discovery rate (FDR), 227 unique malonylation sites within 85 proteins were found to be increased in MCD-deficient tissues ($P_{adjusted} < 0.1$; Table S1). Fold changes for statistically significant hypermalonylation events ranged from quite small (~1.4) to very large (~293). The majority of the hypermalonylated peptides observed in the setting of MCD deficiency (heart; Figure 1F, sk. muscle; Figure S4A; Table S1) mapped to proteins resident within the mitochondrial matrix (Figure 1F; red data points represent mitochondrial targets) (Calvo et al., 2016), consistent with the immunoblots (Figure S2H). When comparing hypermalonylated peptides identified in $MCD^{M-/-}$ hearts versus skeletal muscle, we found 60% overlap at the protein level, but only 32% of unique malonylated peptides identified in each tissue shared a common lysine residue—likely due in part to the stochastic nature of shotgun proteomics data acquisition. Changes in mitochondrial *Kmal* were not accompanied by global alterations in the proteome, assessed via nLC-MS/MS using the unenriched or “input” fractions from each tissue. Thus, other than MCD, only one (DECR1) of the other ~4,700 identified proteins was differentially expressed between $MCD^{fl/fl}$ and $MCD^{M-/-}$ tissues after adjusting for multiple hypothesis testing ($P_{adjusted} < 0.1$). Therefore, increases in malonyl-peptide abundance following MCD deletion were not due to differences in protein expression (heart; Figure 1G, sk. muscle; Figure S4B; Table S1). When adjustment for multiple hypothesis testing was restricted to the mitochondrial proteome, 13 proteins, all in heart tissue, were found to be differentially expressed at this same significance threshold ($P_{adjusted} < 0.1$). Aside from DHRS1 and MCD, which were lower in MCD-deficient hearts, 6 of the 11 increasing proteins participate in mitochondrial beta-oxidation (ACOT2, CPT2, DECR1, DHRS1, ETFDH, and LYRM5). The proteomics results were consistent with immunoblots performed on mitochondrial lysates showing that electron transfer flavoprotein dehydrogenase (ETFDH; Figures S4C and S4D) and HADHA (Figures S4C and S4F) were modestly upregulated in MCD-deficient mitochondria, whereas the expression of ETFA and various ETS subunits were unchanged (Figures S4C, S4E, S4G, and S4H). Taken together, these data suggest the primary consequences of MCD deficiency within the muscle proteome is hypermalonylation of mitochondrial proteins. Proteins modified by malonylation were distributed throughout various mitochondrial pathways, including: acyl CoA metabolism, TCA cycle, ETS, ATP synthesis, amino acid metabolism, reactive oxygen species (ROS) detoxification, protein translation, and CoQ synthesis (Figure 1H).

Functional Assessment of Lysine Malonylation Using a Comprehensive Mitochondrial Diagnostics Assay Platform

The finding of widespread *Kmal* in mitochondria of MCD-deficient muscle tissues, coupled with minimal changes in the mitochondrial proteome and metabolite profiles, provided a unique opportunity to assess the functional impact of these PTMs in a clinically relevant model with functional sirtuin activity. Moreover, the protein targets of malonylation overlapped substantially with those previously identified as hyperacylated in the context of genetically engineered sirtuin deficiencies and/or metabolic diseases. Thus, functional interrogation of the lysine malonylome identified herein was expected to unveil highly susceptible lysine acylation sites that confer important biological consequences. Because malonyl-CoA accumulation and lysine malonylation were greatest in heart tissue, we aimed to comprehensively evaluate the respiratory phenotype of heart mitochondria from $MCD^{M-/-}$ versus control mice. To this end, we used a recently developed bioenergetics assay platform that evaluates respiratory fluxes and energy transfer in intact mitochondria working to regenerate ATP in the context of physiologically relevant energy demands and thermodynamic constraints (Fisher-Wellman et al., 2018). The platform leverages a modified version of the creatine kinase (CK) energetic clamp technique (Figure 2A) to titrate and control the extra-mitochondrial ATP:ADP ratio (i.e., G_{ATP} ; expressed in kcal/mol) to which isolated mitochondria are exposed. In simple terms, the assay platform evaluates how well a given population of mitochondria, energized by a specific combination of carbon fuels, responds to an energy challenge. Transition from a high to low ATP:ADP ratio mimics an increase in energy demand, akin to a transition between rest and exercise, and thereby serves as an *in vitro* “stress test.” Analysis of the linear relationship between energy demand (ATP:ADP, G_{ATP}) and oxygen flux ($\dot{J}O_2$) allows for an estimation of respiratory “conductance” (i.e., reciprocal of resistance), wherein a steeper slope indicates greater sensitivity and improved kinetics. Both the absolute rates of oxygen consumption and respiratory sensitivity (slope) depend on energy gradients and fluxes controlled by three principal regulatory nodes: (1) the dehydrogenase enzymes, (2) the electron transport system (ETS) and, (3) ATP synthesis and transport, which together mediate the transfer of energy from that available in carbon substrates to electron potential energy (G_{redox}) to the proton motive force (PMF, G_{H^+}) to the free energy of ATP hydrolysis (G_{ATP}) (Figure 2B). To gain insight into the free energies that drive the transduction process, we combined the dynamic $\dot{J}O_2$ assays with parallel assessments of membrane potential (Ψ_m), the primary contributor to the PMF, and NAD(P)H/NAD(P)⁺ redox state, along with $\dot{J}H_2O_2$ as a measure of electron leak. A second arm of the assay platform serves to validate and/or further elucidate specific functional perturbations identified within each control node. This is accomplished through direct assessment of maximal ATP synthesis rates ($\dot{J}ATP$) measured in intact mitochondria exposed to various substrates in the context of a hexokinase ADP clamp, as well as carbon flux through multiple DH enzyme activities ($\dot{J}NADH$) performed in alamethicin permeabilized mitochondria that retain organization of protein complexes. Finally, Complex V activity is measured in mitochondrial lysates. Collectively, the entire suite of biochemical assays provides diagnostic information across wide-ranging pathways of the mitochondrial metabolic network.

Creatine Kinase Clamp Assays Reveal Subtle Bioenergetic Consequences of Lysine Malonylation

Use of different substrate combinations in isolated mitochondrial systems allows for the assessment of fluxes across specified spans of the energy transduction network, as each substrate combination results in a predictable activation of a subset of DH enzymes and ETS components. For example, saturating concentrations of pyruvate/malate (Pyr/M) will exclusively generate NADH from PDH, IDH3, and MDH2 and activate all three proton pumps within the ETS (e.g., CI, CIII, CIV). By contrast, succinate/rotenone (Succ/R) will restrict dehydrogenase flux to SDH, which generates FADH₂ and activates only 2 of the 3 ETS proton pumps (e.g., CIII, CIV), resulting in decreased respiratory efficiency (P:O ratio; ATP generated per O₂ consumed). For our experiments with heart mitochondria from MCD^{fl/fl} and MCD^{M-/-} mice, respiratory sensitivity was assessed in the presence of saturating doses of glutamate/malate (G/M), Pyr/M, octanoylcarnitine/malate (Oct/M), or Succ/R. Assessment of NAD-linked respiration supported by either G/M or Pyr/M revealed no differences in absolute $\dot{J}O_2$ or respiratory sensitivity between genotypes (Figures 3A and 3E; G/M, Pyr/M). Respiratory sensitivities in the presence of Oct/M and Succ/R were also similar between genotypes (Figures 3A and 3E; Oct/M, Succ/R); however, absolute $\dot{J}O_2$ in the presence of Oct/M was higher in MCD^{M-/-} heart mitochondria for the two lowest ATP-free energy conditions (Figure 3A; Oct/M). Subsequent analysis of maximal respiratory capacity measured with saturating ADP and the long-chain fatty acid substrate, palmitoylcarnitine, were likewise indicative of adaptations that favored flux through beta-oxidation in the MCD^{M-/-} hearts (Figure S5A).

Although the $\dot{J}O_2$ plots were largely unremarkable, parallel assessment of Ψ and NAD(P)H/NAD(P)⁺ redox revealed evidence of genotype-specific mitochondrial remodeling. Thus, regardless of the substrate, Ψ trended toward a hyperpolarized state (Figure 3B) and the relationship between $\dot{J}O_2$ and Ψ shifted rightward, such that mitochondria from MCD^{M-/-} mice were maintaining a greater (more negative) Ψ for a given rate of oxygen consumption (Figure 3D). Despite the hyperpolarized Ψ , NAD(P)H/NAD(P)⁺ redox potential was unchanged (Figure 3C). Taken together, these observations pointed toward more robust matrix DH fluxes and/or a potential flux limitation at node 3 (“ATP synthesis”). It should be noted that in these assays, G_{ATP} is maintained by unlimited capacitance conferred by excess CK and creatine; thus, a phenotype of improved energy transfer efficiency (i.e., more negative Ψ for a given $\dot{J}O_2$) versus heightened resistance at the ATP synthesis node, are indistinguishable without further diagnostic information from the second arm of the platform.

MCD Deficiency Alters Activities of Multiple NAD-Linked Dehydrogenases and ATP Synthase

To further probe the source of the hyperpolarized Ψ in Mcd^{M-/-} heart mitochondria, we next assessed substrate-specific maximal flux through ATP synthase in intact mitochondria, as well as fluxes through multiple NAD-linked DH enzymes using permeabilized mitochondria or mitochondrial lysates, both assayed in a single 96-well plate format. Results revealed consistent increases in pyruvate (PDH), alpha-ketoglutarate (AKGDH) and branched chain ketoacid (BCKDH) DH complexes in MCD^{M-/-} mitochondria, whereas

glutamate DH (GDH), malate DH (MDH) and hydroxyacyl-CoA DH (HADHA) fluxes were unchanged (Figure 3G; \mathcal{NADH}). Assessment of maximal $\mathcal{J}O_2$ using the substrate combination of pyruvate and carnitine, which restricts DH activation to PDH (Muoio et al., 2012), confirmed increased PDH flux capacity in $MCD^{M-/-}$ heart mitochondria (Figure S5C), which was explained in part by diminished phosphorylation of PDHE1A (S232 to a greater extent than S293), an inactivating PTM (Figures S5D and S5E). Because malonyl CoA serves as a precursor for mitochondrial lipoate (Feng et al., 2009), which is used for lipoylation of the E2 subunits of PDH, AKGDH, and BCKDH, we also assessed lipoylation status of these enzymes. However, analysis by immunoblot proved negative (Figures S5F and S5G). Direct measurement of $\mathcal{J}ATP$ synthesis in intact $MCD^{M-/-}$ heart mitochondria revealed slightly decreased ATP synthesis capacity as compared to controls, but only in the presence of Oct/M (Figure 3G; $\mathcal{J}ATP$). Assessment of ATP synthase activity, measured in the reverse direction using mitochondrial lysates, revealed a ~15% decrease in enzyme activity (Figure 3H), providing further evidence that CV might be contributing to a flux limitation in the $MCD^{M-/-}$ mitochondria.

In sum, the combination of heightened DH capacity and a modest resistance at the ATP synthesis node could explain why $MCD^{M-/-}$ heart mitochondria tend to maintain a hyperpolarized Ψ . Nonetheless, this level of ATP synthase inhibition was not sufficient to increase the rate of substrate-supported proton leak in the absence of ADP (Figure S5B) or electron leak measured under the energetic conditions of the CK clamp (Figure 3F). Notably, this set of experiments evaluated respiratory and redox fluxes of >15 metabolic enzymes identified as hypermalonylated proteins in the context of MCD deficiency, and yet the only evidence of impaired function was a modest 15% decline in maximal ATP synthase activity.

Loss of SIRT5 in the Heart Specifically Affects Succinate Dehydrogenase and ATP Synthase

Next, we sought to evaluate a second genetic model characterized by lysine hyperacylation due to total body deletion of the mitochondrial deacylase *Sirt5*. Recent analysis of hearts from the same cohort of *Sirt5* null mice used for the current study showed that relative abundance of over ~2000 unique K_{suc} sites in *Sirt5* KO hearts were increased by a magnitude ranging from 2- to 1,000-fold, with ~70% of those sites exceeding a 5-fold change (Hershberger et al., 2017). These mice have a baseline phenotype (Sadhukhan et al., 2016) as well as increased susceptibility to heart failure induced by transaortic constriction (Hershberger et al., 2017); thus, we expected *Sirt5*^{-/-} mitochondria would manifest clear bioenergetic insufficiencies. Contrary to this prediction, respiration profiles of mitochondria energized with the NAD-linked substrates, G/M and Pyr/M (Figures 4A and 4E; G/M and Pyr/M) were unaffected by genotype, whereas absolute $\mathcal{J}O_2$ and respiratory sensitivities in the presence of FAD-linked substrates, Oct/M and Succ/R, were only modestly reduced in the *Sirt5* KO group (Figures 4A and 4E; Oct/M and Succ/R). In contrast to the $MCD^{M-/-}$ model, membrane potential in *Sirt5*^{-/-} mitochondria was either unchanged or trended toward a more depolarized state, which reached significance only in the context of Succ/R (Figure 4B). Accordingly, plotting $\mathcal{J}O_2$ against Ψ revealed a slight leftward shift, which was particularly evident in the presence of Succ/R (Figure 4D), consistent with Zhang et al. (2017). Analysis of the NAD(P)H/NAD(P)⁺ redox potential showed either no change or

trends toward an increased (more reduced) redox energy charge in the *Sirt5*^{-/-} group (Figure 4C), suggesting NAD-linked DH enzymes were not a source of flux resistance. Electron leak supported by Pyr/M was unaltered by genotype (Figure 4F). Assays of NAD-linked DH enzyme fluxes and maximal *J*ATP (Figure 4G; *J*ATP) rates produced largely negative results, with only one exception; HADHA flux was increased in *Sirt5*^{-/-} mitochondria (Figure 4G; *J*NADH). Similar to that observed in the setting of MCD deficiency, maximal activity of ATP synthase measured in mitochondrial lysates was decreased ~15% in *Sirt5*^{-/-} mitochondria (Figure 4H). Together, these data suggest that the primary impact of hypersuccinylation caused by SIRT5 ablation was a modest disruption of energetic fluxes mediated by protein complexes associated with or positioned in the inner mitochondrial membrane, including the FAD-linked DH complexes (SDH and ETFDH) and ATP synthase.

Loss of SIRT3 in the Heart Minimally Affects Mitochondrial Energetics, Despite Partial Inhibition of ATP Synthase

The most extensively studied mitochondrial sirtuin, the SIRT3 deacetylase, acts on the best characterized acyl modification, lysine acetylation (Kac). The cardiac acetylome of SIRT3-deficient mice was previously shown to encompass over 500 hyperacetylated peptides that exceeded abundance of that in the control group by a factor of 2- to 85-fold (Dittenhafer-Reed et al., 2015; Martin et al., 2017). Moreover, a pool of SIRT3 has been shown to bind ATP synthase (Yang et al., 2016). Thus, to compare the functional consequences of malonylation and succinylation with that of acetylation, the mitochondrial diagnostics workflow was applied to isolated heart mitochondria prepared from mice harboring heart- and muscle-specific deficiency of SIRT3 (*Sirt3*^{M-/-}) as compared to transgenic littermates carrying the floxed alleles (*Sirt3*^{fl/fl}). In *Sirt3*^{M-/-} mitochondria, respiratory sensitivities with all substrate combinations (Figures 5A and 5E), as well as measurements of Ψ (Figures 5B and 5D) and NAD(P)H/NAD(P)⁺ redox (Figure 5C), were universally unaffected by genotype, with the exception of a slight hyperreduced redox state in the presence of G/M at an ATP free energy of -13.95 kcal/mol in *Sirt3*^{M-/-} mitochondria. Electron leak supported by Pyr/M was similarly unaffected by genotype (Figure 5F). Measurements of *J*ATP synthesis revealed a slight increase in *Sirt3*^{M-/-} mitochondria energized with G/M (Figure 5G; *J*ATP). Dehydrogenase fluxes were generally unaffected by genotype, with the exception of a slight decrease in PDH activity (Figure 5G; *J*NADH). Of note, this decline in PDH maximal activity was insufficient to impair pyruvate-supported respiratory sensitivity. Despite a rather unremarkable respiratory phenotype across all substrates, the maximal activity of ATP synthase was again found to be decreased by ~15% in *Sirt3*^{M-/-} mitochondria (Figure 5H). These findings suggest that absent of other bioenergetic perturbations, the modest decline in ATP synthase activity was insufficient to produce a phenotype in respiring mitochondria.

Analysis of the Complex V Acylome by Label-free Quantitative nLC-MS/MS

Given that partial loss of ATP synthase activity was observed in all three genetic models of hyperacylation (Figures 3H, 4H, and 5H), we questioned whether this effect might be mediated by acyl modification of one or more specific lysine residues common to each of the knockout lines analyzed. To test this possibility, the acyl-landscape of CV isolated by Blue Native-PAGE (Figure S6A) was evaluated in each mouse line using label-free

quantitative nLC-MS/MS. This approach yielded 637 proteins identified and quantified across all samples—the top-five most abundant proteins corresponded to known subunits of the ATP synthase complex (ATP5A1, ATP5B, ATP5H, ATP5O, ATP5F1), with an average sequence coverage of 84% (Table S2). Approximately half of the acyl peptides identified and quantified in these samples (~414 quantified peptides) map to known subunits of the ATP synthase complex (~194 CV acyl-peptides; Table S2). The specific acyl modification found to be more abundant in each KO model aligned with expectations based on the genetic deficiency. That is, 8 malonyl-peptides, 28 succinyl-peptides, and 23 acetyl-peptides were found to be increased ($> 1.5 \log_2 \text{FC}$) above wild-type (WT) controls in samples from MCD-, SIRT5-, and SIRT3-deficient mitochondria, respectively (Figures 6A–6C; Table S2) – consistent with previous proteomics work identifying CV as a recurring acylation target across multiple biological models (Basisty et al., 2018; Hosp et al., 2017). Also noteworthy is that the five most robustly upregulated malonylation sites measured by label-free proteomics in semi-purified CV samples from MCD null compared to controls (ATP5L K55, ATP5F1 K225, ATP5O K162, ATP5B K124, ATP5A1 K531; Table S2) also exhibited hyperacylation (FDR $< 10\%$) in the discovery study using the TMT method (Table S1). Although the specific lysine residues found to be differentially acylated in each model mapped to similar protein subunits of CV, not a single overlapping lysine residue was found to be hyperacylated across all three models (Figures 6D and 6E). Lack of overlap could be due in part to incomplete coverage of low abundant PTMs; however, the label-free proteomics methods used for this analysis incorporates algorithms for handling missing data to minimize sampling inconsistencies. In aggregate, these results suggest that the link between hyperacylation and diminished CV activity stems from a series of stochastic events on biochemically vulnerable lysine residues, rather than specifically targeted PTMs. Interestingly, ATP5A1 appeared highly susceptible to protein acylation, as 13 distinct lysine residues of this CV subunit were found to be hyperacylated above wild-type levels across all models (Figure 6E).

Analysis of Mitochondrial Bioenergetics and Complex V Acylation in a Model of Diet-Induced Obesity

Lastly, to compare the genetic models of hyperacylation to a physiologic perturbation known to broadly augment acyl-PTMs (Alrob et al., 2014; Davies et al., 2016a), we analyzed heart mitochondria harvested from mice fed a high fat (HF) diet for 8 weeks as compared to those fed standard chow (SC). Mitochondrial purity was similar between the chow versus HFD preparations (Figures S6B and S6C). Assessment of bioenergetic fluxes showed that the diet caused a generalized decrease in absolute $\dot{V}O_2$, regardless of substrate, and a slight reduction in respiratory sensitivity in the context of the NAD-linked substrates, G/M and Pyr/M (Figures 7A and 7E). Membrane potentials (Figures 7B and 7D) and redox profiles (Figure 7C) were unremarkable; however, exposure to the high fat diet increased rates of electron leak, measured in the presence of Pyr/M and Oct/M (Figure 7F). This effect, which was most prominent during the CK clamp assay, offers evidence that over-nutrition promotes mitochondrial H_2O_2 generation in the context of physiologically relevant energetic conditions.

The forgoing diet-induced changes in JO_2 were accompanied by diminished activity of several DH enzymes (Figure 7G; NADH - PDH, AKGDH, GDH), consistent with slight reductions in NAD-linked supported JATP (Figure 7G; JATP). Notably, the activity of ATP synthase was unaffected by diet (Figure 7G; CV), even though we identified several acyl PTMs on the complex that were increased in abundance in the context of the HFD versus the standard chow condition (Figure 7H). Compared to the genetic loss-of-function models, diet-induced changes in the lysine acylome of CV were less striking, ranging from 1- to 10-fold on a linear scale, and consisted mainly of acetyl-lysine modifications (Table S2). When comparing hyperacylated residues increased by the HFD ($> 1.5 \log_2 \text{FC}$, relative to chow fed control) to those identified in the genetic models, we found only 5 lysine residues (Atp5a1 K103, K161, K498, and K531; Atp5b K259) in common. Thus, taken together, the impact of the diet on the overall mitochondrial respiratory phenotype was more remarkable than the sirtuin-deficient models, whereas its effect on the CV acyl-landscape was less impressive. These findings argue against a major role for acyl-PTMs in mediating diet-induced alterations in mitochondrial function.

DISCUSSION

Identification of thousands of unique, stress-responsive lysine acylation sites distributed throughout the mitochondrial proteome has been facilitated by the advent of high-resolution mass spectrometry instruments able to detect low stoichiometric PTMs (Hosp et al., 2017). Although the breadth of these modifications is clearly impressive, a growing number of studies have concluded that the vast majority of acyl PTMs occur at occupancy rates of less than 1% (Nakayasu et al., 2014; Weinert et al., 2014, 2015). Similar to most acyl-proteome studies, the current investigation measured and reported relative amounts of detected acyl-peptides rather than absolute quantities. Because the majority of mitochondrial-derived acyl-peptides detected by mass spectrometry are present at low occupancy, a significant change in the context of a KO model might have little biological relevance. Thus, although mitochondrial acyl-PTMs are emerging as ultra-sensitive biomarkers of mitochondrial acyl CoA content and/or flux, increasing recognition of their low stoichiometries has raised uncertainties about their roles as bona fide metabolic regulators (Fernandez-Marcos et al., 2012; Peterson et al., 2018; Weinert et al., 2015). An alternative theory suggests sirtuins function as constitutively active quality control enzymes that preserve normal function of mitochondrial proteins by continuously repairing nonenzymatic acylation (Weinert et al., 2015). This model implies that the stress sensitivities resulting from sirtuin deficiencies are a consequence of disrepair, which in turn compromises mitochondrial performance and metabolic resilience in the face of an energy challenge. Nonetheless, regardless of whether sirtuins act in a regulatory capacity and/or as a repair mechanism, convincing evidence that protein hyperacylation per se does indeed cause mitochondrial dysfunction in animal models is lacking.

Among the barriers to progress in this field is the lack of highly sensitive and widely accessible assay platforms for comprehensive assessment of carbon flux and energy transduction in isolated mitochondrial systems. For this reason, functional validation of acyl PTMs has relied heavily on enzyme activity assays, often comparing 0% versus near 100% stoichiometry modeled with mutant constructs designed to mimic the impact of a specific

modification on protein biochemistry and/or structure (Bharathi et al., 2013; Chen et al., 2011; Fernandes et al., 2015; Hallows et al., 2006; Hebert et al., 2013; Schlicker et al., 2008; Schwer et al., 2006; Shimazu et al., 2010; Still et al., 2013; Yang et al., 2015; Yu et al., 2012; Zhao et al., 2010). Moreover, functional validation is typically pursued using a candidate approach focused on one enzyme or pathway, assayed in isolation. The primary drawback of this approach is that it precludes assessment of potential cumulative effects and cooperativity (Baeza et al., 2016), referring to the collective impact of multiple PTMs across the entire mitochondrial network.

By contrast, insights revealed by the present study stem from application of a recently developed bioenergetics assay platform designed to bridge the gap between molecular and functional mitochondrial phenomics (Fisher-Wellman et al., 2018). Compared to conventional respirometry methods, the multiplexed assay platform enables more comprehensive and less biased assessment of respiratory fluxes and energy transfer, performed under dynamic and more physiologically relevant energetic conditions. The collective results of these assays inform a “diagnostic tree” that localizes a given change in respiratory sensitivity and/or efficiency to one or more potential sites of regulation that can be further probed by more targeted assays (Figure S7). Application of this platform to a functional comparison of heart mitochondria from three distinct genetic models of mitochondrial hyperacylation revealed few or no deficits in a large number of respiratory and enzymatic fluxes, despite relative increases in acyl-PTM abundance that exceeded 100-fold. Moreover, the present study found very little evidence that NAD-linked DH fluxes per se were reduced in the settings of three distinct models of wide-ranging hyperacylation. One caveat to consider is that the assays employed did not measure Michaelis-Menten kinetics of specific enzymes. Still, a prominent theme emerging from this field of study is that increased acylation of the mitochondrial proteome—by malonylation, succinylation and/or acetylation—imposes negative feedback on DH enzymes involved in beta-oxidation (Colak et al., 2015; Sadhukhan et al., 2016), which in turn increases risk of hepatic and/or cardiac pathologies (Bharathi et al., 2013; Hirschey et al., 2010; Zhang et al., 2015). These findings appear to conflict with those of the current study. However, the strongest evidence linking hyperacylation to diminished beta-oxidation comes from assays using radiolabeled palmitate and CO₂ trapping performed in tissue homogenates or isolated mitochondria, or assessment of maximal respiration supported by fatty acid substrates. Importantly, diminished rates of CO₂ production and/or maximal respiration could reflect flux limitations imposed at any number of steps throughout the mitochondrial energy transduction process, including complex V.

Interestingly, the only biochemical phenotype identified in all three of the genetic models tested in this study was a ~15% decline in ATP synthase activity, which corresponded with increased acylation of multiple lysine residues on protein constituents of CV. By comparison, in the context of a physiological model of mitochondrial acyl CoA accumulation (e.g., HFD), hyperacylation of CV was more modest and biochemical evidence of compromised ATP synthase activity and/or flux was lacking. In fact, contrary to that seen in the genetic models, the most prominent mitochondrial flux alteration caused by the HFD was elevated electron leak (i.e., \dot{H}_2O_2 emission). Although perturbations at the ATP synthesis control node (ANT or the phosphate carrier) could contribute to increased

H_2O_2 emission, the preponderance of evidence suggests that elevated electron leak induced by high fat feeding arises from alterations within the ETS (Anderson et al., 2009). Moreover, assessment of the precise lysine residues found to be modified within CV, determined by label-free proteomics, failed to provide any evidence of specificity. These results are consistent with the idea that severe circumstances (e.g., genetic deficiencies) can push non-enzymatic lysine acylation to a level that interferes with the conformation of large protein complexes, particularly those associated with the inner mitochondrial membrane.

In summary, the present study sought to interrogate the functional relevance of cardiac acyl PTMs by applying a recently developed bioenergetics assay platform to a diverse set of mouse models harboring hyperacylation of mitochondrial proteins in heart. Taken at face value, our findings suggest the vast majority of mitochondrial acyl PTMs have little or no impact on respiratory function, which aligns with another recent report examining the role of Sirt3 in the pancreatic beta-cell (Peterson et al., 2018). The primary consequence of robust proteome-wide increases in relative acyl-lysine occupancy rates within the matrix of cardiac mitochondria appears to be a modest decline in maximal activity of ATP synthase, due to the collective effects of several non-specific modifications. We consider several explanations for results that appear to contradict the prevailing narrative in this field. First, perhaps the stoichiometry of the PTMs in the models tested herein did not reach that occurring in the context of organ stress, such as heart failure or type 2 diabetes. Although possible, it seems unlikely that the stoichiometry of the most functionally relevant PTMs in the context of normal physiology or pathophysiology exceeds that which occurs in these complete loss-of-function models (Baeza et al., 2016; Hebert et al., 2013). Second, the cumulative impact of multiple non-enzymatic acylation events on ATP synthase, and other membrane-associated complexes, could prove detrimental as a “second hit” in the context of chronic metabolic disorders that severely compromise respiratory capacity. Third, the acyl-proteome landscape could impact interactions between the mitochondrial reticulum and other organelles and/or cellular constituents, which would not be captured in our assay system. Lastly, the findings raise the intriguing possibility that sirtuins evolved not to protect against the ravages of lysine acylation, but rather to act as rheostats that modulate carbon catabolism in proportion to overall flux through deacylation reactions, which consume NAD^+ and therefore have the potential to impose feedback on specific DH enzymes by altering the local redox environment. This might explain how multiple low stoichiometric acyl PTMs that spread across enzymes and complexes of a specific metabolic pathway contribute to flux control without having a direct impact on protein conformation and function. To this point, deacylase flux would be similarly low in sirtuin-deficient mitochondria as compared to a control group with minimal lysine acylation, thereby producing a similar bioenergetic phenotype. Further examination of these possibilities now awaits future study.

STAR*METHODS

CONTACT FOR REAGENT AND RESOURCE SHARING

Further information and requests for resources and reagents should be directed to and will be fulfilled by the Lead Contact, Deborah M. Muoio (debbie.muio@duke.edu).

EXPERIMENTAL MODEL AND SUBJECT DETAILS

All animal studies were approved by the Duke University Institutional Animal Care and Use Committee. C57Bl6 ES cells containing a conditionally targeted *Mlycd* gene were purchased from the KOMP (NIH-funded Knockout Mouse Project) repository at the University of California and homozygous C57BL6-LoxMlycdtm (MCD-loxP) were generated by Dr. David Olson. Appropriate targeting of exon 2 of *Mlycd* was confirmed at both the 5' and 3' ends of the gene using long range PCR. Targeted ES cells were then injected into C57Bl6 blastocysts and implanted in pseudopregnant females. Offspring were genotyped for the presence of the 3' loxP site. The final loxP-flanked, conditional *Mlycd* allele was ultimately generated after removing the Frt-flanked, lacZ:neomycin resistance cassette by crossing with Rosa26-Flp mice. Removal of the Frt-flanked lacZ:neomycin cassette was confirmed by PCR. The MCD floxed mice were bred to B6.FVB (129S4)-Tg(Ckmm-cre)^{5Khn/J} (The Jackson Laboratory; #006475). This pairing and subsequent backcrossing to C57BL/6NJ mice produced the floxed control MCD^{fl/fl} and littermate muscle specific MCD knockout mice C57BL6/NJ-LoxMlycd^{tmMuo/Duke} mouse referred to herein as MCD^{M-/-}.

Whole-body knockouts for *Sirt5* (*Sirt5*^{-/-}) were described in Hershberger et al. (2017). Muscle specific *Sirt3* knockout mice (*Sirt3*^{M-/-}) were generated by breeding *Sirt3* floxed mice (*Sirt3*^{fl/fl}) with MCK-Cre mice and backcrossed onto the C57BL/6NJ background. For the high fat diet studies, C57BL/6NJ mice (purchased from Jackson Labs; Stock #005304) were fed a 45% high fat (Research Diets; Cat# D12451) or chow diet for a period of 8 weeks. All mice were housed in a temperature (22°C) and light controlled (12 hour light/12 hour dark) room and given free access to food and water. Male mice were used for all studies with an age range of 10-20 weeks for experiments investigating MCD, *Sirt3* and *Sirt5* deficiency. Experiments involving high fat fed C57BL/6NJ mice were performed on male mice ages 20-26 weeks. Unless otherwise stated, mice were fasted 1 hour and anesthetized with Nembutal (intraperitoneal injection; 100mg/kgBW) prior to tissue removal.

METHOD DETAILS

Chemical & Reagents: Unless otherwise stated, all chemicals were purchased from Sigma-Aldrich. Potassium pyruvate was purchased from Combi-Blocks (QA-1116). Potassium NADP⁺ was purchased from Ark-Pharm (AK671068). Amplex Ultra Red, and Tetramethylrhodamine methyl ester (TMRM) were purchased from Thermo Fisher Scientific. Creatine kinase from rabbit muscle was purchased from Roche Life Science.

Indirect Calorimetry—The Comprehensive Lab Animal Monitoring System (CLAMS, Columbus Instruments) was used to determine rates of oxygen consumption (VO₂), carbon dioxide production (VCO₂) and respiratory exchange ratio (RER). Body weights of all mice were recorded prior to entering the metabolic chambers, as well as at the conclusion of the 36hr protocol. The first 12hrs of the protocol was considered an acclimatization period and thus data from this time period was not included in the final analysis. Whole body VO₂ data were normalized to body weight. Access to food and water during these experiments was *ad libitum*.

Mitochondrial Isolation—Differential centrifugation was employed to prepare isolated mitochondria from skeletal muscle and heart. The following buffers were utilized for all isolations: Buffer A – (phosphate buffered saline (pH = 7.4), supplemented with EDTA(10mM); Buffer B – MOPS (50mM; pH = 7.1), KCl (100mM), EGTA (1mM), MgSO₄ (5mM); Buffer C – Buffer B, supplemented with bovine serum albumin (BSA; 2g/L). Skeletal muscle and heart were excised and immediately placed in ice-cold Buffer A. All tissues were minced and subjected to a 5-minute incubation on ice in Buffer A, supplemented with 0.05% trypsin. Following trypsin incubation, skeletal muscle and heart suspensions were centrifuged at 200 × G for 5-minutes at 4°C to remove trypsin. Tissue pellets were next suspended in Buffer C and then homogenized via a Teflon pestle and borosilicate glass vessel. Tissue homogenates were centrifuged at 500 × G for 10-minutes at 4°C. Supernatant from each tissue was then filtered through thin layers of gauze and subjected to an additional centrifugation at 10,000 × G for 10-minutes at 4°C. Mitochondrial pellets were washed in 1.4 mL of Buffer B, transferred to microcentrifuge tubes and centrifuged at 10,000 × G for 10-minutes at 4°C. Buffer B was aspirated from each tube and final mitochondrial pellets were suspended in 100-200 μL of Buffer B. Protein content was determined via the Pierce BCA protein assay. Functional assays involving isolated mitochondria were carried out in the following buffers; Buffer D – Potassium-MES (105 mM; pH = 7.2), KCl (30 mM), KH₂PO₄ (10 mM), MgCl₂ (5 mM), EGTA (1 mM), BSA (2.5 g/L); Buffer E – HEPES (20 mM; pH = 8.0), KCl (100 mM), KH₂PO₄ (2.5 mM), MgCl₂ (2.5 mM), Glycerol (1%).

Metabolomics—Whole-quadriceps skeletal muscle and heart were powdered under liquid N₂, aliquoted, lysed in appropriate buffer [(50% 2-propanol, 50% 0.1 M KH₂ PO₄, pH 4.45; 0.3 M perchloric acid (used for the measurement of malonyl-CoA)] using a Tissue Lyzer II (QIAGEN), and subjected to metabolomics analysis using stable isotope dilution techniques. Amino acids and acylcarnitine were measured as described previously (An et al., 2004; Wu et al., 2004) using a Waters Acquity UPLC system equipped with a TQD and MassLynx 4.1 operating system. Acyl-CoA esters were extracted as 50 mg/ml tissue lysates, purified, and analyzed as described previously (Magnes et al., 2005; Minkler et al., 2008). Acyl-CoAs were analyzed by flow injection analysis using positive electrospray ionization on a Waters Xevo TQS, employing methanol/water (80:20%, v/v) containing 30 mM NH₄ OH as the mobile phase. Malonyl-CoA was assessed as described previously (Gao et al., 2007) on a Waters Xevo TQ-S mass spectrometer coupled to Acquity UPLC system. Spectra were acquired in the multichannel acquisition mode monitoring the neutral loss of 507 atomic mass units (phosphoadenosine diphosphate) and scanning from m/z 750 to 1060. Heptadecanoyl-CoA was employed as an internal standard for long-chain and very-longchain CoA esters. CoAs were quantified using authentic saturated (C0-C18) and unsaturated (C16:1, C18:2, C18:1, and C20:4) acyl-CoA calibrators. All reported CoAs were within detection limits of the assay. Corrections for heavy isotope effects, mainly ¹³C, to the adjacent 2 spectral peaks were made empirically by referring to the observed spectra for the analytical standards.

Preparation of mouse tissue for western blotting—Flash frozen powdered quadriceps and heart tissue, as well as isolated mitochondrial pellets from each tissue were

thawed on ice and homogenized in CellLytic M (Sigma-Aldrich; Cat# C2978) supplemented with protease inhibitor cocktail and 10 mM nicotinamide using a motor-drive Potter-Elvehjem tissue grinder. Samples were centrifuged at $14,000 \times g$ for 10 min at 4°C and the supernatant saved and frozen at -80°C until later analysis. Protein concentration was determined via the BCA method and the samples were diluted in CellLytic M buffer. Forty micrograms of protein sample were combined with $5\times$ loading buffer and resolved by SDS-PAGE, transferred to nitrocellulose, blocked for ~ 1 hr in 5% milk prepared with TBS followed by western blotting with specific antibodies. Antibodies employed herein were: MCD (Proteintech; #15265-1-AP), Sirt5 (see Key Resources Table), malonyl-lysine (Cell Signaling; #14942), ETFDH (Abcam; #ab126576), ETF α (Abcam; #ab110316), Hadha (Abcam; #ab203114), OXPHOS cocktail (Abcam; #ab110413), Pdhe1 α (Abcam; #ab168379), phosphorylated Pdhe1 α (Serine 232; #AP1063, Serine 293; #AP1062).

Cell lysis, protein digestion, and peptide labeling for TMT proteomics: Skeletal muscle (approximately 20 mg of pulverized skeletal muscle (Quadriceps) and heart (left and right ventricles) tissue from MCD^{fl/fl} and MCD^{MCK^{+/+}} mice ($n = 3/\text{group}$) were resuspended in ice-cold 8M Urea Lysis Buffer (8 M urea in 40 mM Tris, pH 8.0, 30 mM NaCl, 1 mM CaCl₂, $1\times$ cComplete ULTRA mini EDTA-free protease inhibitor tablet, 10 mM Nicotinamide) and the samples were disrupted with a TissueLyzer (QIAGEN) for one minute at 30 Hz. The Samples were frozen on dry ice and thawed for three freeze-thaw cycles and further disrupted by sonication with a probe sonicator in three 5 s bursts (power setting of 3). Samples were centrifuged at $10,000 \times g$ for 10 min at 4°C and the supernatant was retained. Protein concentration was determined by BCA, and equal amount of protein (500 μg , adjusted to 2.5mg/mL with Urea Lysis Buffer) from each sample were reduced with 5 mM DTT at 37°C for 30 min, cooled to room temperature, alkylated with 15 mM iodoacetamide for 30 min in the dark and unreacted iodoacetamide quenched by the addition of DTT up to 15 mM. Initial digestion was performed with Lys C (Wako Chemicals; Cat# 125-05061; 1:100 w:w; 5 μg enzyme per 500 μg protein) for 4 hours at 37°C . Following dilution to 1.5M urea with 40 mM Tris (pH 8.0), 30 mM NaCl, 1 mM CaCl₂, the samples were digested with trypsin (Promega; Cat# V5113; 50:1 w/w, protein:enzyme) overnight at 37°C . The samples were acidified to 0.5% TFA and centrifuged at $4000 \times g$ for 10 min at 4°C to pellet insoluble material. The supernatant containing soluble peptides was desalted on a 50 mg tC18 SEP-PAK Solid Phase Extraction (SPE) column (Waters; Cat# WAT054955) and eluted once with 500 μL 25% acetonitrile/0.1% TFA and twice with 500 μL 50% acetonitrile/0.1% TFA. The 1.5 mL eluate was frozen and dried in a speed vac. The six samples from each tissue were re-suspended in 100 μL of 200 mM triethylammonium bicarbonate (TEAB), mixed with a unique 6-plex Tandem Mass Tag (TMT) reagent (0.8 mg re-suspended in 50 μL 100% acetonitrile), and shaken for 4 hours at room temperature (ThermoFisher Scientific; Cat# 90064). After samples were quenched with 0.8 μL 50% hydroxylamine and shaken for 15 additional minutes at room temperature, all six samples from each tissue were combined, frozen, and dried in a speed vac overnight. The mixtures from each tissue were re-suspended in ~ 1 mL of 0.5% TFA and subjected to SPE again as described above, but with a 100 mg tC18 SEP-PAK SPE column (Waters; Cat# WAT023590). The eluate was vortexed and split into one aliquot containing $\sim 5\%$ of the total peptide mixture (150 μg) and a second aliquot containing $\sim 95\%$ (2.85 mg). Both aliquots

were frozen and dried in a speed vac. The 150 μg aliquot of the “input” material was saved at -80°C for quantification of unmodified peptides and the 2.85 mg aliquot was used for enrichment of malonyl-peptides using immunoprecipitation.

Malonylpeptide enrichment for TMT proteomics—One hundred mg of concentrated Malonyl-Lysine [Mal-K] MultiMab Rabbit mAb mix (Cell Signaling #14942) was coupled to 20 mL of Protein A/G agarose (ThermoFisher; Cat# 20421) in PBS (pH 7.4) in a total volume of 500 μL with gentle rocking overnight at 4°C . The next day, antibody-coupled agarose was pelleted via centrifugation at $2000 \times g$ for 30 s. The supernatant was discarded and pellet washed four times in 1 mL PBS. The dried down TMT-labeled peptides from each tissue were solubilized in 1.4 mL of IAP buffer (Cell Signaling Technology, #9993) and incubated with the Mal-K antibody coupled agarose on a rotator overnight at 4°C . The next day, the antibody-peptide complexes were pelleted via centrifugation at $2000 \times g$ for 30 s and washed 2 times in 1 mL of IAP buffer and three times with ultrapure de-ionized H_2O . The peptides were eluted in 55 μL of 0.1% TFA for 10 min followed by a wash in 50 μL of 0.1% TFA and the supernatants ($2000 \times g$, 30 s) from each elution were combined. The eluate was acidified to 0.5% TFA (and brought to a 1 mL volume), desalted on a 50 mg tC18 SEP-PAK SPE column as described above, frozen, and dried in a speed vac.

nLC-MS/MS for TMT proteomics—All samples were subjected to nanoLC-MS/MS analysis using either a nano-Acquity (Waters) or an EASY-nLC UPLC system (Thermo Fisher Scientific) coupled to a Q Exactive Plus Hybrid Quadrupole-Orbitrap mass spectrometer (Thermo Fisher Scientific) via a nano-electrospray ionization source. Prior to injection, malonylpeptide sample was resuspended in 12 μL 0.1% formic acid and was analyzed with at least technical duplicate runs. For each injection of 4 μL , the sample was first trapped on a Symmetry C18 20 mm \times 180 μm trapping column (5 $\mu\text{L}/\text{min}$ at 99.9/0.1 v/v water/acetonitrile), after which the analytical separation was performed over a 90-minute gradient (flow rate of 400 nanoliters/minute) of 3 to 30% acetonitrile using a 1.7 μm Acquity BEH130 C18 75 μm \times 250 mm column (Waters Corp.), with a column temperature of 55°C . MS¹ (precursor ions) was performed at 70,000 resolution, with an AGC target of 1×10^6 ions and a maximum injection time (IT) of 60 ms. MS² spectra (product ions) were collected by data-dependent acquisition (DDA) of the top 20 most abundant precursor ions with a charge greater than 1 per MS¹ scan, with dynamic exclusion enabled for a window of 30 s. Precursor ions were filtered with a 1.2 m/z isolation window and fragmented with a normalized collision energy (NCE) of 30. MS² scans were performed at 17,500 resolution, with an AGC target of 1×10^5 ions and a maximum IT of 60 ms.

Data analysis for TMT proteomics—Proteome Discoverer 2.2 (PDv2.2) was used for raw data analysis, with default search parameters including oxidation (15.995 Da on M) as a variable modification and carbamidomethyl (57.021 Da on C) and TMT6plex (229.163 Da on peptide N-term and K) as fixed modifications, and 2 missed cleavages (full trypsin specificity). To assess labeling efficiency as a quality control measure, the input fraction was re-searched with N-terminal TMT as a variable modification, confirming N-terminal labeling of 79 and 94% of all PSMs from the skeletal muscle and heart samples, respectively. Malonyl-enriched fraction runs added malonylation (86.00039 Da on K) as a

variable modification and changed TMT to a variable modification on K (remaining fixed on peptide N-term) and increased maximum missed trypsin cleavage sites to 4. Considering each data type (malonyl, input) separately, PSMs from each search algorithm were filtered to a 1% FDR and PTM site localization probabilities were determined. PSMs were grouped to unique peptides while maintaining a 1% FDR at the peptide level and using a 90% localization threshold for PTMs. Peptides from all fractions (malonyl, input) were grouped to proteins together using the rules of strict parsimony and proteins were filtered to 1% FDR using the Protein FDR Validator node of PD2.2. Reporter ion intensities for all PSMs having co-isolation interference below 0.5 (50% of the ion current in the isolation window) and an average S/N > 2.5 for reporter ions were summed together at the peptide and protein level, but keeping quantification for each data type (malonyl, input) separate. Peptides shared between protein groups were excluded from protein quantitation calculations.

Statistical analysis for TMT proteomic experiment—Protein and peptide groups tabs in the PDv2.2 results were exported as tab delimited .txt. files, and analyzed with an in-house *Python* module based on a previously described workflow (McDonnell et al., 2016). First, peptide group reporter intensities for each peptide group in the input material were summed together for each TMT channel, each channel's sum was divided by the average of all channels' sums, resulting in channel-specific loading control normalization factors to correct for any deviation from equal protein/peptide input into the six sample comparison. Reporter intensities for peptide groups from the malonylpeptide runs, and for proteins from the input fraction runs were divided by the tissue-specific loading control normalization factors for each respective TMT channel. Analyzing the malonylpeptide, and protein datasets separately (for each tissue), all loading control-normalized TMT reporter intensities were converted to \log_2 space, and the average value from the six samples was subtracted from each sample-specific measurement to normalize the relative measurements to the mean. For MCD^{fl/fl} and MCD^{M-/-} comparisons (n = 3) within each tissue, condition average, standard deviation, p value (p, two-tailed Student's t test, assuming equal variance), and adjusted p value ($P_{adjusted}$ Benjamini Hochberg FDR correction) were calculated (Benjamini and Hochberg, 1995; Lesack and Naugler, 2011). For protein-level quantification, only Master Proteins—or the most statistically significant protein representing a group of parsimonious proteins containing common peptides identified at 1% FDR—were used for quantitative comparison. Malonylpeptide measurements were calculated both alone (referred to as *abundance*) and with normalization to any change in the corresponding Master Protein (referred to as *relative occupancy*), calculated by subtracting \log_2 Master Protein values from PTM-containing peptide quantitation values on a sample-specific basis.

Blue Native-PAGE—Mitochondrial pellets were lysed in 1 × Native gel electrophoresis sample buffer (BisTris; pH = 7.2, NaCl, glycerol and Ponceau S; Thermo #BN2003), supplemented with 10 mM nicotinamide, 1x protease inhibitor cocktail and 6% digitonin. Samples were left on ice for ~20 minutes and then spun down at 10,000 × G for 30 minutes at 4°C. Supernatants were transferred to fresh micro-centrifuge tubes and protein content was determined using the BCA assay. Prior to loading samples onto Native gels, G-250 Coomassie sample additive (Thermo #BN2004) was added to each sample. Native-PAGE was performed by loading 50 ug of mitochondrial protein onto a 4%-16% BisTris Native gel

(Thermo; BN1004). Following PAGE, proteins were fixed and de-stained (40% methanol, 10% acetic acid) for ~10 minutes at room temperature.

CV Acylome Sample Prep—Mitochondrial pellets were lysed in 1 × Native gel electrophoresis sample buffer (BisTris; pH = 7.2, NaCl, glycerol and Ponceau S; Thermo #BN2003), supplemented with 10 mM nicotinamide, 1× protease inhibitor cocktail and 6% digitonin. Samples were left on ice for ~20 minutes and then spun down at 10,000 × G for 30 minutes at 4°C. Supernatants were transferred to fresh micro-centrifuge tubes and protein content was determined using the BCA assay. Prior to loading samples onto Native gels, G-250 Coomassie sample additive was added to each sample. Native-PAGE was performed by loading 50 µg of mitochondrial protein onto a 4%–16% BisTris Native gel. Following PAGE, proteins were fixed and de-stained (40% methanol, 10% acetic acid) for ~10 minutes at room temperature. Following Blue Native-PAGE, the bands corresponding to CV were excised using a scalpel and chopped into 1.5² mm cubes. Gel pieces were washed 1 × for 15 minutes in 100 µLs of 1:1 Acetonitrile (ACN;100%):100mM ammonium bicarbonate (AmBIC). Solution was removed and gel pieces were washed in 100 µLs of 100% ACN. Following ACN removal, gel pieces were rehydrated and reduced in 100 mM AmBIC, supplemented with 10mM dithiothreitol (DTT) for 30 minutes at 55°C. Solution was removed and replaced with 100mM AmBIC, supplemented with 55mM iodoacetamide and samples were incubated for 30 minutes at room-temperature protected from light. Gel pieces were washed 1 × for 15 minutes in 100 µLs of 1:1 ACN/AmBIC and then again in 100 µLs of 100% ACN. Following removal of ACN, gel pieces were rehydrated in 100 µLs of digestion buffer (50 mM AmBIC, 5 mM CaCl₂, 10 ng/µL trypsin) and incubated overnight at 37°C. Following a brief spin-down, supernatant (containing all peptides) from each sample was placed in fresh 1.7ml tube. Gel pieces were incubated for 15 minutes in 50% ACN, 0.3% formic acid, as well as 80% ACN, 0.3% formic acid. Supernatants from these incubations were combined with the original supernatant. Samples were flash frozen and then speed vacuumed overnight. Dried down peptides were reconstituted in 10 µLs of 5% ACN, 0.1% TFA (pH < 3) and desalted using C18 Ziptips (Millipore; Cat# ZTC18S096) according to manufacturer instructions. Following sample elution, samples were once again dried in a speed vac.

CV Acylome nLC-MS/MS—Samples were resuspended in 20 µLs of 0.1% formic acid and subjected to nLC-MS/MS in a randomized order (with blanks in between) as described above, but with the following changes: For nLC using an EASY-nLC UPLC system (Thermo Fisher Scientific), sample injections of 8.5 µL were first trapped on an Acclaim PepMap 100 C18 trapping column (3 µm particle size, 75 µm × 20 mm) with 22 µL of solvent A (0.1% FA) at a variable flow rate dictated by max pressure of 500 Bar, after which the analytical separation was performed over a 105 minute gradient (flow rate of 300 nL/minute) of 5 to 40% solvent B (90% ACN, 0.1% FA) using an Acclaim PepMap RSLC C18 analytical column (2 µm particle size, 75 µm × 500 mm column (Thermo Fischer Scientific) with a column temperature of 55°C. MS¹ used 70,000 resolution, 3×10⁶ AGC target, and 100 ms maximum IT. MS² used DDA (top 20), dynamic exclusion for 30 s, 1.2 *m/z* isolation window, NCE of 27, 17,500 resolution, 1×10⁵ AGC target, and 100 ms maximum IT. Raw data were processed in PDv2.2 using the Byonic search engine (Protein Metrics, Inc.) as a

node (Bern et al., 2012). To generate a focused database for subsequent acyl-peptide quantification, data were searched against the UniProt mouse proteome database indicated above. Following generation of the focused database using Byonic, all searches included the following four variable modifications (all set as “common”): oxidation (M) and acylation of lysine (monoisotopic additions to K in parentheses) with an acetyl (42.010565 Da), malonyl (86.00039 Da), or succinyl (100.016044 Da) group. Searches for the diet study additional included crotonyl (68.026215), glutaryl (114.031694) and propionyl (56.026215) modifications on K, but these PTMs were not included in post-search data reduction. Fixed modification of carbamidomethyl (C) was selected. The maximum number of missed cleavages was set at 2 and enzyme specificity was trypsin. PSMs were filtered to a 1% false discovery rate (FDR) in PDv2.2 based on the target-decoy search results from Byonic. PSMs were grouped to peptides maintaining 1% FDR at the peptide level and peptides were grouped to proteins using the rules of strict parsimony. Proteins were filtered to 1% FDR using the Protein FDR Validator node of PD2.2. Peptide quantification was done using the MS1 precursor intensity. Imputation was performed via low abundance resampling. Quantitation for each acylpeptide identified was normalized to the relative abundance of the corresponding protein within each sample to control for differences in protein expression, sample loading, and LC-MS performance

Mitochondrial Respiratory Control—High-resolution O₂ consumption measurements were conducted using the Oroboros Oxygraph-2K (Oroboros Instruments). All experiments were carried out at 37°C in a 2 mL reaction volume. Steady-state oxygen consumption rates ($\dot{V}O_2$) ranging from near state 4 (i.e., non-phosphorylating) all the way to ~95% of maximal state 3 were sequentially determined within individual experiments using a modified version of the creatine energetic clamp technique (Glancy et al., 2013; Messer et al., 2012). In this assay, the free energy of ATP hydrolysis (G'_{ATP}) can be calculated based on known amounts of creatine (Cr), phosphocreatine (PCr) and ATP in combination with excess amounts of creatine kinase (CK) and the equilibrium constant for the CK reaction (i.e., K'_{CK}). Calculation of G'_{ATP} was performed according to the following formula:

$$\Delta G'_{ATP} = \Delta G'^{\circ}_{ATP} + RT \ln \frac{[Cr][P_i]}{[PCr][K'_{CK}]}$$

where G'°_{ATP} is the standard apparent transformed Gibbs energy (under a specified pH, ionic strength, free magnesium and pressure), R is the gas constant (8.3145 J/kmol) and T is temperature in kelvin (310.15). Given that experiments were performed via sequential additions phosphocreatine, both the G'°_{ATP} and K'_{CK} were determined at each titration step based on the changes in buffer ionic strength and free magnesium, as previously described (Golding et al., 1996; Teague et al., 1996). Calculation of G'_{ATP} at each titration point was performed using a recently developed online tool (<https://dmpio.github.io/bioenergetic-calculators/>).

Buffer for all assays was Buffer D, supplemented creatine (Cr; 5 mM), phosphocreatine (PCr; 1 mM) and creatine kinase (CK; 20 U/mL). Buffer D for Experiments with Sirt3^{fl/fl} also included ATP (5 mM) prior to the addition of substrates. To begin, isolated

mitochondria (0.025 mg/mL) were added to assay buffer, followed by the addition of respiratory substrates then ATP (5 mM). The following substrate conditions were tested: [Octanoyl-carnitine/Malate – (Oct/M; 0.2/2.5 mM), Glutamate/Malate – (G/M; 10/2.5 mM), Pyruvate/Malate-(Pyr/M; 5/2.5 mM), Succinate/Rotenone-(Succ/R; 10/0.005 mM)]. Following substrate additions, sequential additions of PCr to 3, 6, 9, 12, 15mM were performed to gradually slow $\dot{V}O_2$ back toward baseline. For experiments in which a near state 4 rate were determined, ATP was omitted from the initial buffer and added after the addition of respiratory substrates. Plotting the calculated $\dot{V}O_2$ against the corresponding $\dot{V}O_2$ reveals a linear force-flow relationship, the slope of which represents the conductance/elasticity of the entire respiratory system under specified substrate constraints.

Mitochondrial membrane potential (Ψ) and NAD(P)H/NAD(P)⁺

Redox: Fluorescent determination of Ψ and NAD(P)H/NAD(P)⁺ were carried out simultaneously via a QuantaMaster Spectrofluorometer (QM-400; Horiba Scientific). Determination of Ψ via TMRM was done as described previously (Scaduto and Grotyohann, 1999), via taking the fluorescence ratio of the following excitation/emission parameters [Ex/Em, (572/590 nm)/(551/590 nm)]. The 572/551nm ratio was then converted to millivolts via a KCl standard curve performed in the presence of valinomycin (Krumshnabel et al., 2014). NAD(P)H excitation/emission parameters were 340/450nm. All experiments were carried out at 37°C in a 0.2 mL reaction volume. Buffer for all assays was Buffer D, supplemented with creatine (Cr; 5mM), phosphocreatine (PCr; 1 mM), creatine kinase (CK; 20 U/mL) and TMRM (0.2 mM). To begin, isolated mitochondria (0.1 mg/mL) were added to the assay buffer, followed by the addition of respiratory substrates (Oct/M, G/M, Pyr/M, Succ/R), adenosine triphosphate (5 mM), and then sequential PCr additions to a final of 3, 6, 9, 12, 15, 18, 21, 24, 30mM. Following the final PCr addition, cyanide (4 mM) was added to induce a state of 100% reduction within the NAD(P)H/NAD(P)⁺ couple. The fluorescence (Ex/Em, 340/450 nm) signal recorded in the presence of mitochondria alone without respiratory substrates was used as the 0% reduction state for the NAD(P)H/NAD(P)⁺ couple. NAD(P)H/NAD(P)⁺ during the entire experiment was expressed as a percentage reduction according to the following formula: % Reduction = $(F - F_{0\%}) / (F_{100\%} - F_{0\%})$.

Mitochondrial JH₂O₂ Emission: Mitochondrial H₂O₂ emission was measured fluorometrically via the Amplex Ultra Red (AUR)/horseradish peroxidase (HRP) detection system (Ex:Em 565:600 nm). Fluorescence was monitored via a QuantaMaster Spectrofluorometer (QM-400, Horiba Scientific). For each experiment, resorufin fluorescence was converted to pmoles H₂O₂ via an H₂O₂ standard curve generated under identical substrate conditions as employed for each protocol. All experiments were carried out at 37°C in a 0.2 mL reaction volume. Buffer for all assays was Buffer D, supplemented with creatine (Cr; 5 mM), phosphocreatine (PCr; 1 mM), creatine kinase (CK; 20 U/mL), AUR (10 μ M), HRP (1 U/mL) and superoxide dismutase (20U/mL). To begin, isolated mitochondria (0.1 mg/mL) were added to assay buffer, followed by the addition of respiratory substrates (Oct/M and Pyr/M), auranofin (0.1 μ M), adenosine triphosphate (5 mM), and then sequential PCr additions to a final of 6, and 15 mM. The percentage of electron leak is calculated by dividing the rate of H₂O₂ production by the corresponding O₂ consumption rate measured under identical conditions and expressed as a percentage (%)

Leak = \dot{H}_2O_2/\dot{O}_2). Of note, the \dot{H}_2O_2 rates used in the calculation were generated in the presence of auranofin; however, the corresponding \dot{O}_2 assays did not contain auranofin, as the inhibitor does not impact respiratory conductance (Fisher-Wellman et al., 2018).

JATP Synthesis—Rates of ATP synthesis were determined as described previously (Lark et al., 2016). Buffer for the assay was Buffer D, supplemented with glucose (5 mM), hexokinase (1 U/mL), glucose-6-phosphate dehydrogenase (G6PDH; 2 U/mL), NADP⁺ (2 mM) and ADP (0.2 mM). Assay buffer (200 μ L) was loaded into individual wells of a 96-well plate, followed by isolated mitochondria (2 μ g/well). The assay was initiated with the addition of respiratory substrates following a ~5 minute pre-incubation at 37°C in the absence of substrates to deplete endogenous metabolites. In the assay, NADPH and ATP are produced in a 1:1 stoichiometry and thus JATP was determined via monitoring the NADPH auto-fluorescence (Ex:Em 340/450nm) signal. Fluorescence values were converted to pmoles of ATP via an ATP standard curve. The following substrate conditions were tested in parallel for each assay [Oct/M; 0.2/2.5 mM, G/M; 10/2.5 mM, Pyr/M; 5/2.5 mM, Succ/R; 10/0.005 mM].

JNADH Production—Rates of NADH production were determined as described previously (Fisher-Wellman et al., 2013). Buffer for the assays was Buffer D, supplemented with alamethicin (0.03 mg/mL), rotenone (0.005 mM) and NAD⁺ (2 mM) or NADP⁺ (2 mM). For experiments designed to assess JNADH from the pyruvate dehydrogenase complex (PDH), the alpha-ketoglutarate dehydrogenase complex (AKGDH) and the branched-chain keto-acid dehydrogenase complex (BCKDH) the following cofactors were included in the assay: coenzyme A (0.1 mM) and thiamine pyrophosphate (0.3 mM). Assay buffer (200 μ L) was loaded into individual wells of a 96-well plate, followed by isolated mitochondria (2-60 μ g/well). The assay was initiated with the addition of enzymatic substrates. In the assay, NADH is determined via auto-fluorescence (Ex:Em 340/450nm). Fluorescence values were converted to pmoles of NADH via an NADH standard curve. The following substrates were tested in parallel for each assay [pyruvate (5 mM), alpha ketoglutarate (10 mM), α -keto- β -methylvalerate (5 mM), glutamate (10 mM) and malate (5 mM)].

CV Activity Assay—Mitochondrial lysates for the assay were prepared via dilution of the final isolated mitochondrial suspensions in CellLytic M at a protein concentration of 2mg/mL. Buffer for the assay was Buffer E, supplemented with lactate dehydrogenase/pyruvate kinase (10 U/mL), phosphoenoyl-pyruvate (5 mM), rotenone (0.005 mM) and NADH (0.2 mM). Assay buffer (200 μ L) was loaded into individual wells of a 96-well plate, followed by mitochondrial lysate (2 μ g/well). Assays were done in the absence and presence of oligomycin (0.005 mM) in order to calculate the oligomycin-sensitive rates of ATP hydrolysis. The assay was initiated with the addition of ATP (5 mM). In the assay, NADH oxidation and ATP hydrolysis occur at a 1:1 stoichiometry and thus CV activity (pmoles of ATP/sec/mg) was determined via tracking the degradation in the NADH auto-fluorescence (Ex:Em 376/450nm) signal upon ATP addition. Fluorescence values were converted to pmoles of NADH via an NADH standard curve.

Hydroxyacyl-CoA Dehydrogenase Activity—Mitochondrial lysates for the assay were prepared via dilution of the final isolated mitochondrial suspensions in CellLytic M at a protein concentration of 2 mg/mL. Buffer for the assay was Buffer E, supplemented with rotenone (0.005 mM) and NADH (0.2 mM). Assay buffer (200 μ L) was loaded into individual wells of a 96-well plate, followed by mitochondrial lysate (5 μ g/well). The assay was initiated with the addition of acetoacetyl-CoA (0.2 mM). The activity of hydroxyacyl-CoA dehydrogenase was determined via tracking the degradation in the NADH auto-fluorescence (Ex:Em 340/450 nm) signal upon acetoacetyl-CoA addition. Fluorescence values were converted to pmoles of NADH via an NADH standard curve.

QUANTIFICATION AND STATISTICAL ANALYSIS

Data are presented as mean \pm SEM. Statistical analysis was performed using t tests or one-way ANOVA with Student-Newman-Keuls methods for analysis of significance among groups. Figures were generated using GraphPad Prism (Version 7.0). The level of significance was set at $p < 0.05$. Statistical details of each experiment are located in the figure legends. Unless otherwise stated, the number of mice per experiment is represented by “N.”

DATA AND SOFTWARE AVAILABILITY

All raw data for proteomics experiments is available online using accession number “PXD011375” for Proteome Xchange (Deutsch et al., 2017) and accession number “JPST000507” for jPOST Repository (Okuda et al., 2017).

Supplementary Material

Refer to Web version on PubMed Central for supplementary material.

ACKNOWLEDGMENTS

This work was supported by the NIH (F32DK105665 to K.H.F.-W.; F30DK1085602 to M.T.D.; F32DK105922 to A.S.W.; R01DK089312 and 2P01DK058398 to D.M.M.; 1R01HL128349 to D.M.M. and D.P.K.) and the American Heart Association (18CDA34110216 to P.A.G.). We thank Brian Glancy, Wayne Willis, and Robert Balaban for developing the original prototype of the CK clamp method.

REFERENCES

References

- Alrob OA, Sankaralingam S, Ma C, Wagg CS, Fillmore N, Jaswal JS, Sack MN, Lehner R, Gupta MP, Michelakis ED, et al. (2014). Obesity-induced lysine acetylation increases cardiac fatty acid oxidation and impairs insulin signalling. *Cardiovasc. Res* 103, 485–497. [PubMed: 24966184]
- An J, Muoio DM, Shiota M, Fujimoto Y, Cline GW, Shulman GI, Koves TR, Stevens R, Millington D, and Newgard CB (2004). Hepatic expression of malonyl-CoA decarboxylase reverses muscle, liver and whole-animal insulin resistance. *Nat. Med* 10, 268–274. [PubMed: 14770177]
- Anderson EJ, Lustig ME, Boyle KE, Woodlief TL, Kane DA, Lin C-T, Price JW 3rd, Kang L, Rabinovitch PS, Szeto HH, et al. (2009). Mitochondrial H₂O₂ emission and cellular redox state link excess fat intake to insulin resistance in both rodents and humans. *J. Clin. Invest* 119, 573–581. [PubMed: 19188683]
- Baeza J, Smallegan MJ, and Denu JM (2016). Mechanisms and dynamics of protein acetylation in mitochondria. *Trends Biochem. Sci* 41, 231–244. [PubMed: 26822488]

- Basisty N, Meyer JG, Wei L, Gibson BW, and Schilling B (2018). Simultaneous quantification of the acetylome and succinylome by ‘one-pot’ affinity enrichment. *Proteomics* 18, e1800123. [PubMed: 30035354]
- Benjamini Y, and Hochberg Y (1995). Controlling the false discovery rate: a practical and powerful approach to multiple testing. *J. R. Stat. Soc. B* 57, 289–300.
- Bern M, Kil YJ, and Becker C (2012). Byonic: advanced peptide and protein identification software. *Curr. Protoc. Bioinformatics* Chapter 13, Unit 13.20.
- Bharathi SS, Zhang Y, Mohsen AW, Uppala R, Balasubramani M, Schreiber E, Uechi G, Beck ME, Rardin MJ, Vockley J, et al. (2013). Sirtuin 3 (SIRT3) protein regulates long-chain acyl-CoA dehydrogenase by deacetylating conserved lysines near the active site. *J. Biol. Chem* 288, 33837–33847. [PubMed: 24121500]
- Calvo SE, Clauser KR, and Mootha VK (2016). MitoCarta2.0: an updated inventory of mammalian mitochondrial proteins. *Nucleic Acids Res.* 44 (D1), D1251–D1257. [PubMed: 26450961]
- Chen Y, Zhang J, Lin Y, Lei Q, Guan KL, Zhao S, and Xiong Y (2011). TumorsuppressorSIRT3 deacetylates and activates manganese superoxide dismutase to scavenge ROS. *EMBO Rep.* 12, 534–541. [PubMed: 21566644]
- Colak G, Pougovkina O, Dai L, Tan M, Te Brinke H, Huang H, Cheng Z, Park J, Wan X, Liu X, et al. (2015). Proteomic and biochemical studies of lysine malonylation suggest its malonic aciduria-associated regulatory role in mitochondrial function and fatty acid oxidation. *Mol. Cell. Proteomics* 14, 3056–3071. [PubMed: 26320211]
- Davies MN, Kjalarsdottir L, Thompson JW, Dubois LG, Stevens RD, Ilkayeva OR, Brosnan MJ, Rolph TP, Grimsrud PA, and Muoio DM (2016a). The acetyl group buffering action of carnitine acetyltransferase offsets macronutrient-induced lysine acetylation of mitochondrial proteins. *Cell Rep.* 14, 243–254. [PubMed: 26748706]
- Deusch EW, Csordas A, Sun Z, Jarnuczak A, Perez-Riverol Y, Ternent T, Campbell DS, Bernal-Llinares M, Okuda S, Kawano S, et al. (2017). The ProteomeXchange consortium in 2017: supporting the cultural change in proteomics public data deposition. *Nucleic Acids Res* 45, D1100–D1106. [PubMed: 27924013]
- Dittenhafer-Reed KE, Richards AL, Fan J, Smallegan MJ, Fotuhi Siahpirani A, Kemmerer ZA, Prolla TA, Roy S, Coon JJ, and Denu JM (2015). SIRT3 mediates multi-tissue coupling for metabolic fuel switching. *Cell Metab.* 21, 637–646. [PubMed: 25863253]
- Du Y, Cai T, Li T, Xue P, Zhou B, He X, Wei P, Liu P, Yang F, and Wei T (2015). Lysine malonylation is elevated in type2diabetic mouse models and enriched in metabolic associated proteins. *Mol. Cell. Proteomics* 14, 227–236. [PubMed: 25418362]
- Feng D, Witkowski A, and Smith S (2009). Down-regulation of mitochondrial acyl carrier protein in mammalian cells compromises protein lipoylation and respiratory complex I and results in cell death. *J. Biol. Chem* 284, 11436–11445. [PubMed: 19221180]
- Fernandes J, Weddle A, Kinter CS, Humphries KM, Mather T, Szweda LI, and Kinter M (2015). Lysine acetylation activates mitochondrial aconitase in the heart. *Biochemistry* 54, 4008–4018. [PubMed: 26061789]
- Fernandez-Marcos PJ, Jenning EH, Canto C, Harach T, de Boer VCJ, Andreux P, Moullan N, Pirinen E, Yamamoto H, Houten SM, et al. (2012). Muscle or liver-specific Sirt3 deficiency induces hyperacetylation of mitochondrial proteins without affecting global metabolic homeostasis. *Sci. Rep* 2, 425. [PubMed: 22645641]
- Fisher-Wellman KH, Gilliam LAA, Lin C-T, Cathey BL, Lark DS, and Darrell Neuffer P (2013). Mitochondrial glutathione depletion reveals a novel role for the pyruvate dehydrogenase complex as a key H₂O₂-emitting source under conditions of nutrient overload. *Free Radic. Biol. Med* 65, 1201–1208. [PubMed: 24056031]
- Fisher-Wellman KH, Davidson MT, Narowski TM, Lin CT, Koves TR, and Muoio DM (2018). Mitochondrial diagnostics: a multiplexed assay platform for comprehensive assessment of mitochondrial energy fluxes. *Cell Rep.* 24, 3593–3606.e10. [PubMed: 30257218]
- Gao L, Chiou W, Tang H, Cheng X, Camp HS, and Burns DJ (2007). Simultaneous quantification of malonyl-CoA and several other short-chain acyl-CoAs in animal tissues by ion-pairing reversed-phase HPLC/MS. *J. Chromatogr. B. Anal. Technol. Biomed. Life Sci.* 853, 303–313.

- Glancy B, Willis WT, Chess DJ, and Balaban RS (2013). Effect of calcium on the oxidative phosphorylation cascade in skeletal muscle mitochondria. *Biochemistry* 52, 2793–2809. [PubMed: 23547908]
- Golding EM, Teague WEJ, and Dobson GP (1996). Adjustment of K' to varying pH and pMg for the creatine kinase, adenylate kinase and ATP hydrolysis equilibria permitting quantitative bioenergetic assessment. *J. Exp. Biol* 198, 1775–1782.
- Hallows WC, Lee S, and Denu JM (2006). Sirtuins deacetylate and activate mammalian acetyl-CoA synthetases. *Proc. Natl. Acad. Sci. USA* 103, 10230–10235. [PubMed: 16790548]
- Hebert AS, Dittenhafer-Reed KE, Yu W, Bailey DJ, Selen ES, Boersma MD, Carson JJ, Tonelli M, Balloon AJ, Higbee AJ, et al. (2013). Calorie restriction and SIRT3 trigger global reprogramming of the mitochondrial protein acetylome. *Mol. Cell* 49, 186–199. [PubMed: 23201123]
- Hershberger KA, Abraham DM, Martin AS, Mao L, Liu J, Gu H, Locasale JW, and Hirschey MD (2017). Sirtuin 5 is required for mouse survival in response to cardiac pressure overload. *J. Biol. Chem* 292, 19767–19781. [PubMed: 28972174]
- M D, Shimazu T, Goetzman E, Jing E, Schwer B, Lombard DB, Grueter CA, Harris C, Biddinger S, Ilkayeva OR, et al. (2010). SIRT3 regulates mitochondrial fatty-acid oxidation by reversible enzyme deacetylation. *Nature* 464, 121–125. [PubMed: 20203611]
- Horton JL, Martin OJ, Lai L, Riley NM, Richards AL, Vega RB, Leone TC, Pagliarini DJ, Muoio DM, Bedi KC Jr., et al. (2016). Mitochondrial protein hyperacetylation in the failing heart. *JCI Insight* 2, e84897. [PubMed: 26998524]
- Hosp F, Lassowskat I, Santoro V, DeVleeschauwer D, Fliegner D, Redestig H, Mann G, Christian S, Hannah MA, and Finkemeier I (2017). Lysine acetylation in mitochondria: from inventory to function. *Mitochondrion* 33, 58–71. [PubMed: 27476757]
- Kim SC, Sprung R, Chen Y, Xu Y, Ball H, Pei J, Cheng T, Kho Y, Xiao H, Xiao L, et al. (2006). Substrate and functional diversity of lysine acetylation revealed by a proteomics survey. *Mol. Cell* 23, 607–618. [PubMed: 16916647]
- Koentges C, Pfeil K, Schnick T, Wiese S, Dahlbock R, Cimolai MC, Meyer-Steenbuck M, Cenkerova K, Hoffmann MM, Jaeger C, et al. (2015). SIRT3 deficiency impairs mitochondrial and contractile function in the heart. *Basic Res. Cardiol* 110, 36. [PubMed: 25962702]
- Koves TR, Ussher JR, Noland RC, Slentz D, Mosedale M, Ilkayeva O, Bain J, Stevens R, Dyck JRB, Newgard CB, et al. (2008). Mitochondrial overload and incomplete fatty acid oxidation contribute to skeletal muscle insulin resistance. *Cell Metab.* 7, 45–56. [PubMed: 18177724]
- Krumschnabel G, Eigentler A, Fasching M, and Gnaiger E (2014). Use of safranin for the assessment of mitochondrial membrane potential by high-resolution respirometry and fluorometry. *Methods Enzymol.* 542, 163–181. [PubMed: 24862266]
- Kulkarni RA, Worth AJ, Zenggeya TT, Shrimp JH, Garlick JM, Roberts AM, Montgomery DC, Sourbier C, Gibbs BK, Mesaros C, et al. (2017). Discovering targets of non-enzymatic acylation by thioester reactivity profiling. *Cell Chem. Biol* 24, 231–242. [PubMed: 28163016]
- Lantier L, Williams AS, Williams IM, Yang KK, Bracy DP, Goelzer M, James FD, Gius D, and Wasserman DH (2015). SIRT3 is crucial for maintaining skeletal muscle insulin action and protects against severe insulin resistance in high-fat-fed mice. *Diabetes* 64, 3081–3092. [PubMed: 25948682]
- Lark DS, Torres MJ, Lin C-T, Ryan TE, Anderson EJ, and Neuffer PD (2016). Direct real-time quantification of mitochondrial oxidative phosphorylation efficiency in permeabilized skeletal muscle myofibers. *Am. J. Physiol. Cell Physiol* 311, C239–C245. [PubMed: 27335172]
- Lesack K, and Naugler C (2011). An open-source software program for performing Bonferroni and related corrections for multiple comparisons. *J. Pathol. Inform* 2, 52. [PubMed: 22276243]
- Magnes C, Sinner FM, Regittnig W, and Pieber TR (2005). LC/MS/MS method for quantitative determination of long-chain fatty acyl-CoAs. *Anal. Chem* 77, 2889–2894. [PubMed: 15859607]
- Martin AS, Abraham DM, Hershberger KA, Bhatt DP, Mao L, Cui H, Liu J, Liu X, Muehlbauer MJ, Grimsrud PA, et al. (2017). Nicotinamide mononucleotide requires SIRT3 to improve cardiac function and bioenergetics in a Friedreich's ataxia cardiomyopathy model. *JCI Insight* 2, 93885. [PubMed: 28724806]

- McCain CS, Knotts TA, and Adams SH (2015). Acylcarnitines-old actors auditioning for new roles in metabolic physiology. *Nat. Rev. Endocrinol* 11, 617–625. [PubMed: 26303601]
- McDonnell E, Crown SB, Fox DB, Kitir B, Ilkayeva OR, Olsen CA, Grimsrud PA, and Hirschey MD (2016). Lipids reprogram metabolism to become a major carbon source for histone acetylation. *Cell Rep* 17, 1463–1472. [PubMed: 27806287]
- McGarry JD, Stark MJ, and Foster DW (1978). Hepatic malonyl-CoA levels of fed, fasted and diabetic rats as measured using a simple radioisotopic assay. *J. Biol. Chem* 253, 8291–8293. [PubMed: 711752]
- Messer JI, Jackman MR, Willis WT, Kavazis AN, Smuder AJ, Min K, TGmer N, Powers SK, Lefort N, Glancy B, et al. (2012). Pyruvate and citric acid cycle carbon requirements in isolated skeletal muscle mitochondria. *Am. J. Physiol. Cell Physiol* 286, C565–C572.
- Minkler PE, Kerner J, Ingalls ST, and Hoppel CL (2008). Novel isolation procedure for short-, medium-, and long-chain acyl-coenzyme A esters from tissue. *Anal. Biochem* 376, 275–276. [PubMed: 18355435]
- Muoio DM, Noland RC, Kovalik JP, Seiler SE, Davies MN, DeBalsi KL, Ilkayeva OR, Stevens RD, Kheterpal I, Zhang J, et al. (2012). Muscle-specific deletion of carnitine acetyltransferase compromises glucose tolerance and metabolic flexibility. *Cell Metab.* 15, 764–777. [PubMed: 22560225]
- Nakayasu ES, Wu S, Sydor MA, Shukla AK, Weitz KK, Moore RJ, Hixson KK, Kim J-S, Petyuk VA, Monroe ME, et al. (2014). A method to determine lysine acetylation stoichiometries. *Int. J. Proteomics* 2014, 730725. [PubMed: 25143833]
- Newgard CB (2017). Metabolomics and metabolic diseases: where do we stand? *Cell Metab.* 25, 43–56. [PubMed: 28094011]
- Okuda S, Watanabe Y, Moriya Y, Kawano S, Yamamoto T, Matsumoto M, Takami T, Kobayashi D, Araki N, Yoshizawa AC, et al. (2017). jPOSTrepo: an international standard data repository for proteomes. *Nucleic Acids Res* 45 (D1), D1107–D1111. [PubMed: 27899654]
- Paik WK, Pearson D, Lee HW, and Kim S (1970). Nonenzymatic acetylation of histones with acetyl-CoA. *Biochim. Biophys. Acta.* 213, 513–522. [PubMed: 5534125]
- Peterson BS, Campbell JE, Ilkayeva O, Grimsrud PA, Hirschey MD, and Newgard CB (2018). Remodeling of the acetylproteome by SIRT3 manipulation fails to affect insulin secretion or β cell metabolism in the absence of overnutrition. *Cell Rep.* 24, 209–223.e6. [PubMed: 29972782]
- Poburko D, Santo-Domingo J, and Demaurex N (2011). Dynamic regulation of the mitochondrial proton gradient during cytosolic calcium elevations. *J. Biol. Chem* 286, 11672–11684. [PubMed: 21224385]
- Pougovkina O, Te Brinke H, Wanders RJA, Houten SM, and de Boer VCJ (2014). Aberrant protein acylation is a common observation in inborn errors of acyl-CoA metabolism. *J. Inher. Metab. Dis* 37, 709–714. [PubMed: 24531926]
- Sadhukhan S, Liu X, Ryu D, Nelson OD, Stupinski JA, Li Z, Chen W, Zhang S, Weiss RS, Locasale JW, et al. (2016). Metabolomics-assisted proteomics identifies succinylation and SIRT5 as important regulators of cardiac function. *Proc. Natl. Acad. Sci. USA* 113, 4320–4325. [PubMed: 27051063]
- Scaduto RC Jr., and Grotyohann LW (1999). Measurement of mitochondrial membrane potential using fluorescent rhodamine derivatives. *Biophys. J* 76, 469–477. [PubMed: 9876159]
- Schlicker C, Gertz M, Papatheodorou P, Kachholz B, Becker CFW, and Steegborn C (2008). Substrates and regulation mechanisms for the human mitochondrial sirtuins Sirt3 and Sirt5. *J. Mol. Biol* 382, 790–801. [PubMed: 18680753]
- Schwer B, Bunkenborg J, Verdin RO, Andersen JS, and Verdin E (2006). Reversible lysine acetylation controls the activity of the mitochondrial enzyme acetyl-CoA synthetase 2. *Proc. Natl. Acad. Sci. USA* 103, 10224–10229. [PubMed: 16788062]
- Shimazu T, Hirschey MD, Hua L, Dittenhafer-Reed KE, Schwer B, Lombard DB, Li Y, Bunkenborg J, Alt FW, Denu JM, et al. (2010). SIRT3 deacetylates mitochondrial 3-hydroxy-3-methylglutaryl CoA synthase 2 and regulates ketone body production. *Cell Metab.* 12, 654–661. [PubMed: 21109197]

- Still AJ, Floyd BJ, Hebert AS, Bingman CA, Carson JJ, Gunderson DR, Dolan BK, Grimsrud PA, Dittenhafer-Reed KE, Stapleton DS, et al. (2013). Quantification of mitochondrial acetylation dynamics highlights prominent sites of metabolic regulation. *J. Biol. Chem* 288, 26209–26219. [PubMed: 23864654]
- Teague WEJ Jr., Golding EM, and Dobson GP (1996). Adjustment of K' for the creatine kinase, adenylate kinase and ATP hydrolysis equilibrium varying temperature and ionic strength. *J. Exp. Biol* 199, 509–512. [PubMed: 8930003]
- Ussher JR, Fillmore N, Keung W, Zhang L, Mori J, Sidhu VK, Fukushima A, Gopal K, Lopaschuk DG, Wagg CS, et al. (2016). Genetic and pharmacological inhibition of malonyl CoA decarboxylase does not exacerbate age-related insulin resistance in mice. *Diabetes* 65, 1883–1891. [PubMed: 27207536]
- Wagner GR, and Hirschev MD (2014). Nonenzymatic protein acylation as a carbon stress regulated by sirtuin deacylases. *Mol. Cell* 54, 5–16. [PubMed: 24725594]
- Wagner GR, and Payne RM (2013). Widespread and enzyme-independent Nε-acetylation and Nε-succinylation of proteins in the chemical conditions of the mitochondrial matrix. *J. Biol. Chem* 288, 29036–29045. [PubMed: 23946487]
- Wagner GR, Bhatt DP, O'Connell TM, Thompson JW, Dubois LG, Backos DS, Yang H, Mitchell GA, Ilkayeva OR, Stevens RD, et al. (2017). A class of reactive acyl-CoA species reveals the non-enzymatic origins of protein acylation. *Cell Metab.* 25, 823–837.e8. [PubMed: 28380375]
- Weinert BT, Scholz C, Wagner SA, Iesmantavicius V, Su D, Daniel JA, and Choudhary C (2013a). Lysine succinylation is a frequently occurring modification in prokaryotes and eukaryotes and extensively overlaps with acetylation. *Cell Rep.* 4, 842–851. [PubMed: 23954790]
- Weinert BT, Iesmantavicius V, Wagner SA, Scholz C, Gummesson B, Beli P, Nystrom T, and Choudhary C (2013b). Acetyl-phosphate is a critical determinant of lysine acetylation in *E. coli*. *Mol. Cell* 51, 265–272. [PubMed: 23830618]
- Weinert BT, Iesmantavicius V, Moustafa T, Scholz C, Wagner SA, Magnes C, Zechner R, and Choudhary C (2014). Acetylation dynamics and stoichiometry in *Saccharomyces cerevisiae*. *Mol. Syst. Biol* 10, 716. [PubMed: 24489116]
- Weinert BT, Moustafa T, Iesmantavicius V, Zechner R, and Choudhary C (2015). Analysis of acetylation stoichiometry suggests that SIRT3 repairs nonenzymatic acetylation lesions. *EMBO J.* 34, 2620–2632. [PubMed: 26358839]
- Wu JY, Kao HJ, Li SC, Stevens R, Hillman S, Millington D, and Chen YT (2004). ENU mutagenesis identifies mice with mitochondrial branched-chain aminotransferase deficiency resembling human maple syrup urine disease. *J. Clin. Invest* 113, 434–440. [PubMed: 14755340]
- Yang H, Zhou L, Shi Q, Zhao Y, Lin H, Zhang M, Zhao S, Yang Y, Ling Z-Q, Guan K-L, et al. (2015). SIRT3-dependent GOT2 acetylation status affects the malate-aspartate NADH shuttle activity and pancreatic tumor growth. *EMBO J.* 34, 1110–1125. [PubMed: 25755250]
- Yang W, Nagasawa K, MGNch C, Xu Y, Satterstrom K, Jeong S, Hayes SD, Jedrychowski MP, Vyas FS, Zaganjor E, et al. (2016). Mitochondrial sirtuin network reveals dynamic SIRT3-dependent deacetylation in response to membrane depolarization. *Cell* 167, 985–1000.e21. [PubMed: 27881304]
- Yu W, Dittenhafer-Reed KE, and Denu JM (2012). SIRT3 protein deacetylates isocitrate dehydrogenase 2 (IDH2) and regulates mitochondrial redox status. *J. Biol. Chem* 287, 14078–14086. [PubMed: 22416140]
- Yu J, Sadhukhan S, Noriega LG, Moullan N, He B, Weiss RS, Lin H, Schoonjans K, and Auwerx J (2013). Metabolic characterization of a Sirt5 deficient mouse model. *Sci. Rep* 3, 2806. [PubMed: 24076663]
- Zhang Y, Bharathi SS, Rardin MJ, Uppala R, Verdin E, Gibson BW, and Goetzman ES (2015). SIRT3 and SIRT5 regulate the enzyme activity and cardiolipin binding of very long-chain acyl-CoA dehydrogenase. *PLoS ONE* 10, e0122297. [PubMed: 25811481]
- Zhang Y, Bharathi SS, Rardin MJ, Lu J, Maringer KV, Sims-Lucas S, Prochowik EV, Gibson BW, and Goetzman ES (2017). Lysine desuccinylase SIRT5 binds to cardiolipin and regulates the electron transport chain. *J. Biol. Chem* 292, 10239–10249. [PubMed: 28458255]

- Zhao S, Xu W, Jiang W, Yu W, Lin Y, Zhang T, Yao J, Zhou L, Zeng Y, Li H, et al. (2010). Regulation of cellular metabolism by protein lysine acetylation. *Science* 327, 1000–1004. [PubMed: 20167786]
- Zhou A, Rohou A, Schep DG, Bason JV, Montgomery MG, Walker JE, Grigorieff N, and Rubinstein JL (2015). Structure and conformational states of the bovine mitochondrial ATP synthase by cryo-EM. *eLife* 4, e10180. [PubMed: 26439008]

Author Manuscript

Author Manuscript

Author Manuscript

Author Manuscript

Highlights

- Interrogating the role of lysine acylation in regulating mitochondrial quality
- Comparison of three disparate genetic models of hyperacylated heart mitochondria
- A mitochondrial diagnostics platform evaluates >60 distinct energetic fluxes
- Substantial shifts in the acyl-lysine landscape minimally affect bioenergetics

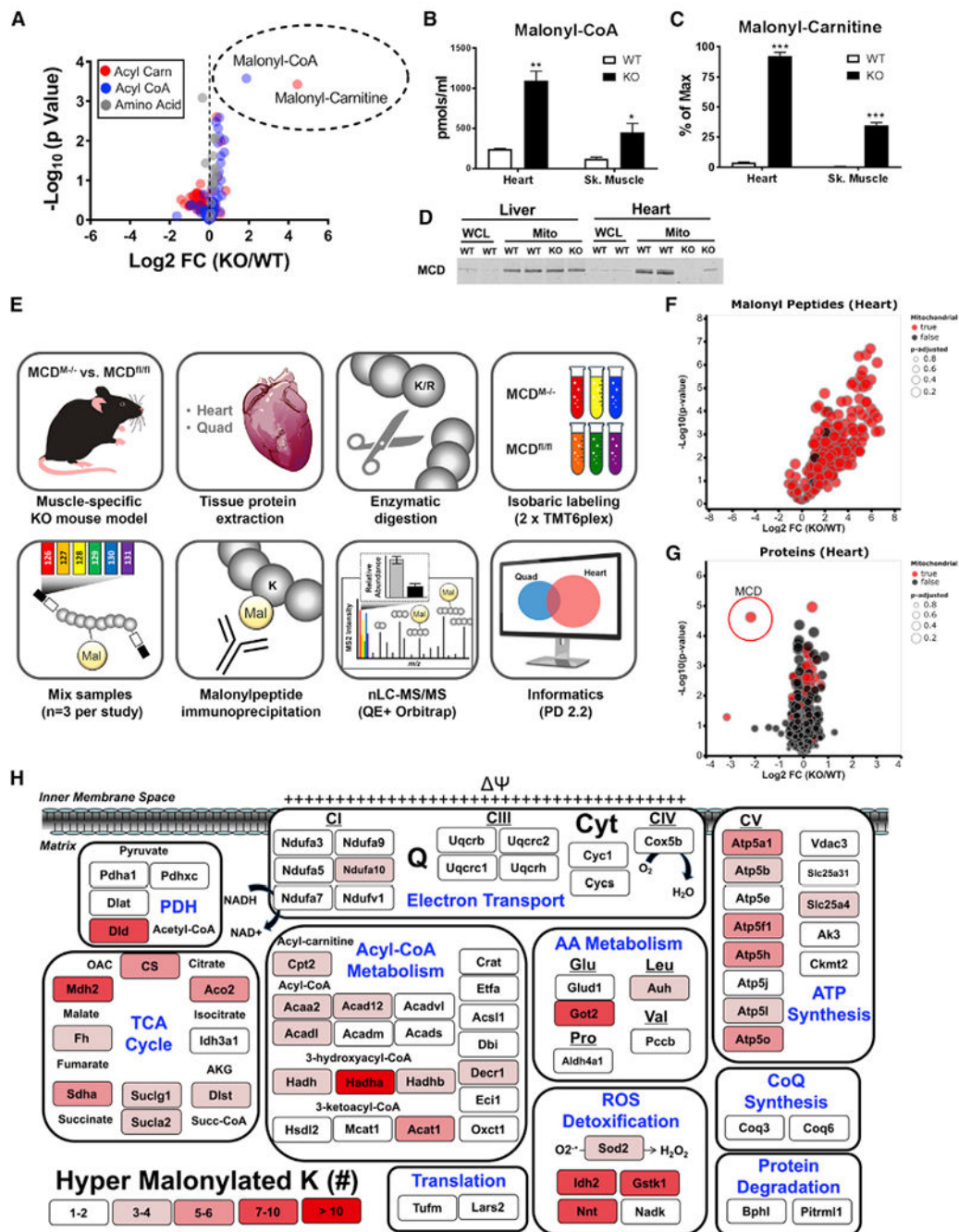


Figure 1. Loss of MCD in Muscle Increases Mitochondrial Malonyl-CoA and Promotes Lysine Malonylation

(A) Volcano plot depicting acyl carnitine (red dots), acyl CoA (blue dots), and amino acid (gray dots) relative abundance in heart of MCD^{fl/fl} (WT) and MCD^{M/-} (KO) mice. Data are expressed as log₂-fold change (KO/WT).

(B) Malonyl CoA abundance.

(C) Malonyl carnitine abundance is expressed as a percentage of MCD^{fl/fl} heart tissue.

(D) MCD expression in liver and heart tissues in whole-cell lysates compared to a mitochondrial-enriched fraction assessed via immunoblot.

(E) Malonyl proteomics workflow.

(F) Volcano plot depicting relative abundance of malonyl-peptides identified in heart tissue from MCD^{fl/fl} and MCD^{M-/-} mice. Red and black dots indicate peptides matched to mitochondrial or non-mitochondrial proteins, respectively. The size of each point is scaled according to its false discovery rate (FDR) such that larger points have lower FDRs.

(G) Volcano plot depicting changes in the heart proteome between genotypes. The data point corresponding to MCD is circled.

(H) hypermalonylated protein targets identified in both heart and skeletal muscle of MCD-deficient mice. Shading of each protein represents the number of hypermalonylated lysine residues ($P_{\text{adjusted}} < 0.1$).

Data are mean \pm SEM. (A–C) n = 6/group, (D) n = 2/group, and (F and G) n = 3/group and were analyzed by Student's t test. *p < 0.05; **p < 0.001; ***p < 0.0001. n represents biological replicates.

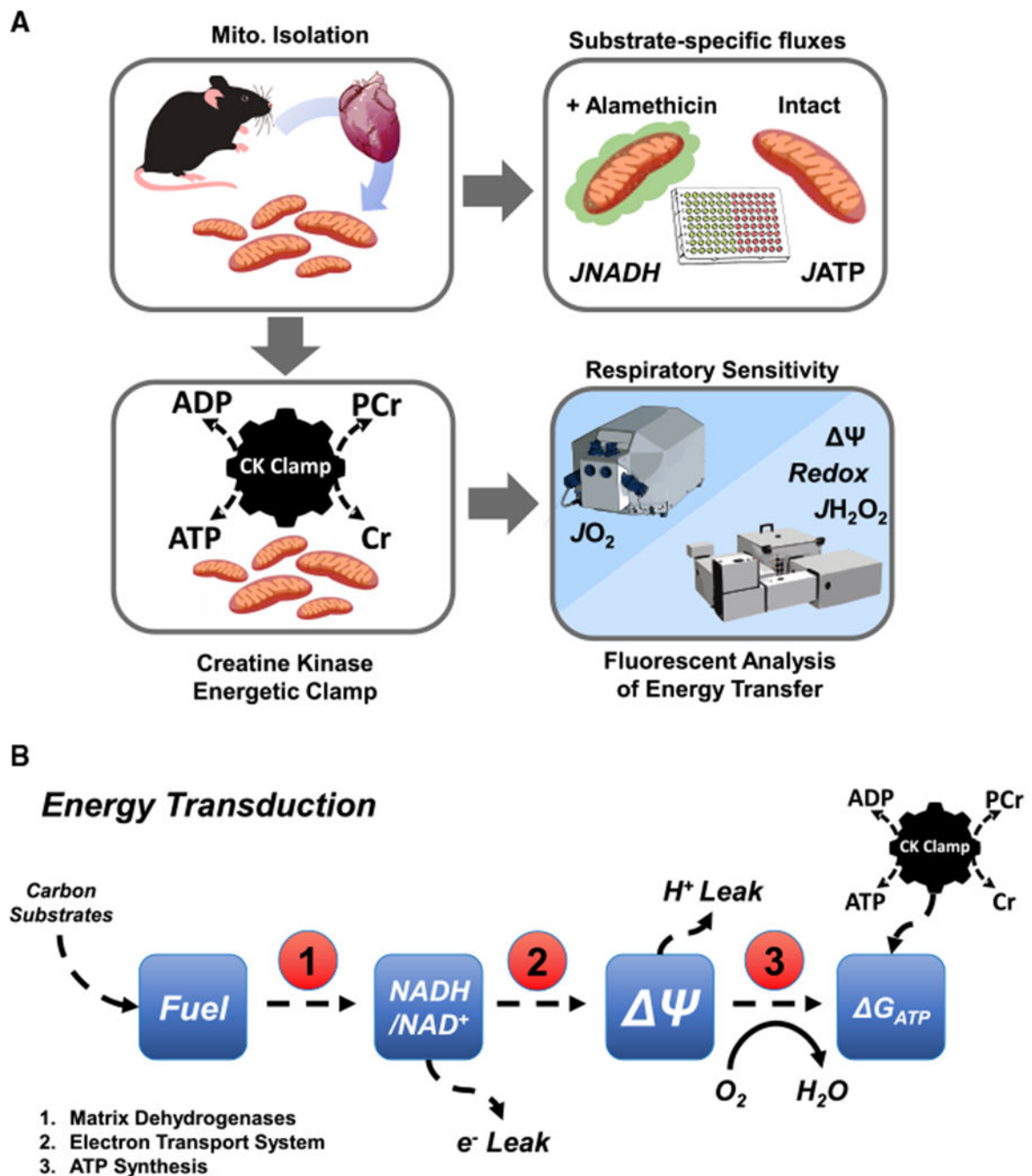


Figure 2. Mitochondrial Diagnostics Workflow

(A) Isolated and intact mitochondria from heart tissue were used for measuring rates of ATP synthesis ($JATP$) or permeabilized (+Alamethicin) for rates of NADH generation ($JNADH$), both performed with multiple substrates in a 96-well plate format. Rates of oxygen consumption (JO_2) and respiratory sensitivity were assessed using the Oroboros-O2K system and the creatine kinase (CK) energetic clamp technique. Parallel measures of membrane potential (Ψ), redox potential (NAD(P)H/NAD(P)⁺), and JH_2O_2 emission were obtained via spectrofluorometric assays using a QuantaMaster Spectrofluorometer.

(B) Mitochondrial energy transduction is modeled as a series of interconnected energy transfer steps that regulate ATP-free energy (G_{ATP}). In node #1, respiratory fuels activate specific dehydrogenase (DH) enzymes that transfer the chemical energy in carbon fuels to electron potential energy (G_{redox}), experimentally assessed via the fluorescent measurement of the NAD(P)H/NAD(P)⁺ redox state. In node #2, the ‘Electron Transport System’ (ETS) converts energy available G_{redox} to proton potential energy (G_{H^+}) harnessed in the electrochemical proton motive force (PMF). Efficiency of energy transfer at node #2 is assessed by fluorescent measurement of Ψ , the primary contributor to the PMF. In node #3, the energy available in G_{H^+} drives the synthesis and transport of ATP via the ATP synthase complex (CV) and the adenine nucleotide translocase (ANT). Mitochondrial $\mathcal{J}O_2$ reflects the flux of the proton current at Complex IV of the ETS and thus serves as the experimental measurement of node #3.

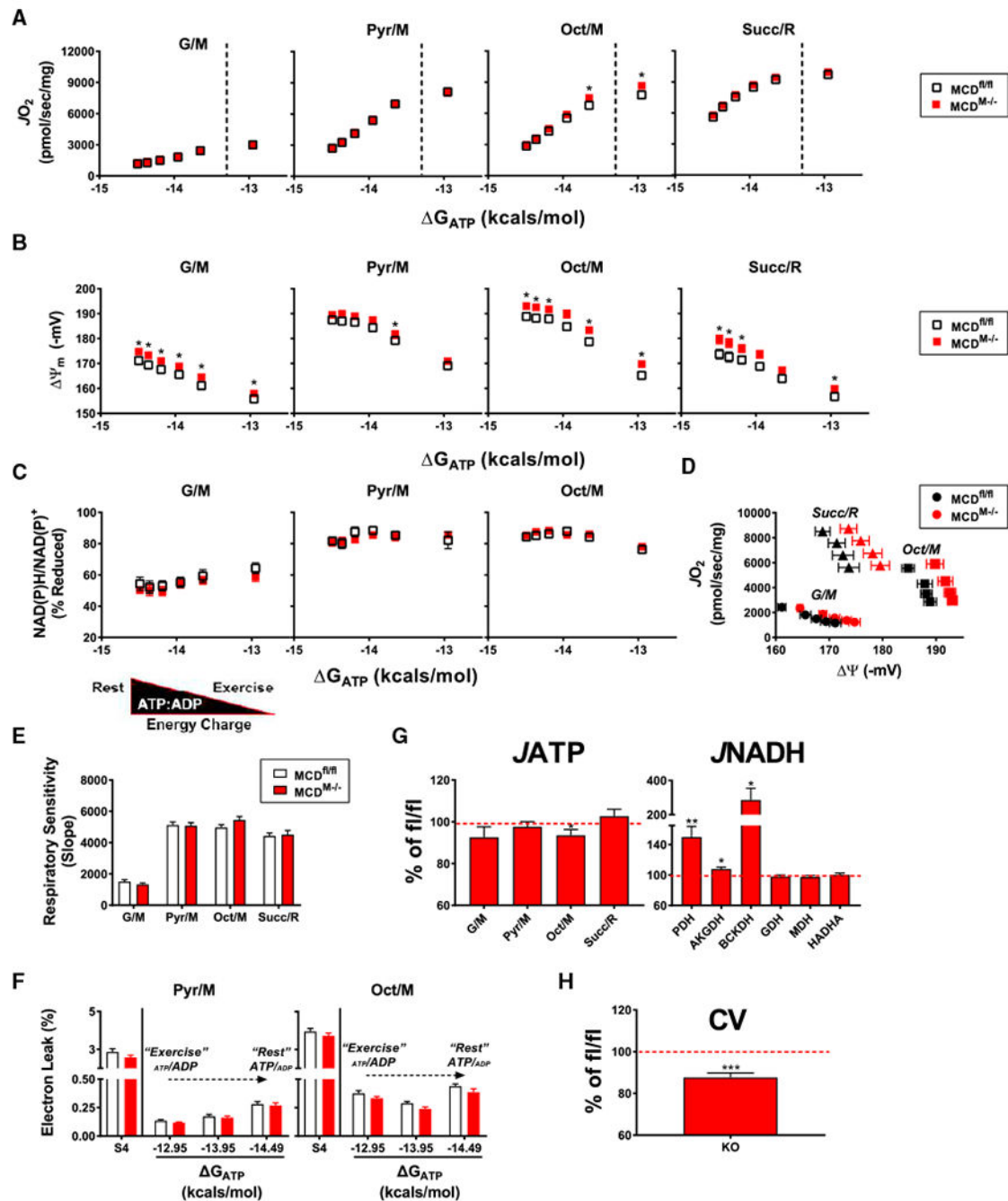


Figure 3. Comprehensive Assessment of Mitochondrial Energy Fluxes in the Setting of MCD Deficiency

(A–H) Isolated mitochondria from hearts of $MCD^{fl/fl}$ versus deficient $MCD^{M-/-}$ mice were used for all experiments.

(A–C) Relationship between mitochondrial (A) J_{O_2} , (B) mitochondrial Ψ , and (C) NAD(P)H/NAD(P)⁺ redoxstate versus Gibb's energy of ATP hydrolysis (ΔG_{ATP}) in mitochondria energized with G/M, Pyr/M, Oct/M, and Succ/Rot.

(D) Mitochondria J_{O_2} plotted against Ψ in the presence of G/M, Succ/R, and Oct/M.

(E) Calculated slopes from the linear portions of the data depicted in (A). Linear portions are located to the left of the dotted line on each graph.

(F) Mitochondria electron leak, expressed as a percentage ($J_{H_2O_2}/JO_2 \times 100 = \% \text{ electron leak}$) in the presence Pyr/M and Oct/M.

(G) Quantified rates of ATP synthesis (J_{ATP}) in intact mitochondria energized with G/M, Pyr/M, Oct/M, and Succ/R; rates of NADH production (J_{NADH}) by various enzymes were measured in permeabilized mitochondria. Data are expressed as the percentage of MCD^{fl/fl} controls.

(H) Quantified CV activity are expressed as the percentage of fl/fl controls.

Data are mean \pm SEM, n = 8–12/group and were analyzed by Student's t test. *p < 0.05; **p < 0.001; ***p < 0.0001. n represents biological replicates.

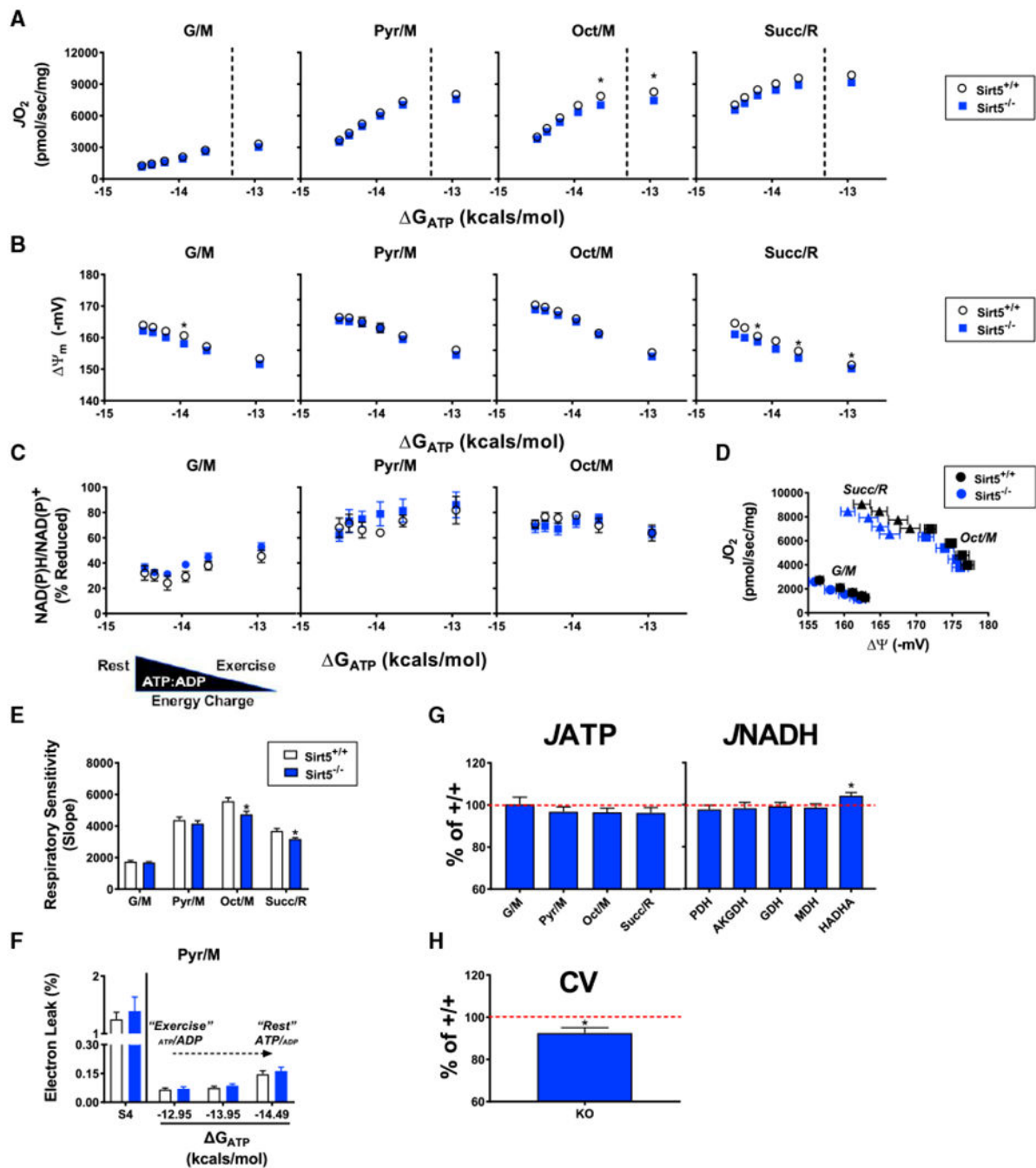


Figure 4. Comprehensive Assessment of Mitochondrial Energy Fluxes in the Setting of Sirt5 Deficiency

(A–H) Isolated mitochondria from hearts of Sirt5 control (Sirt5^{+/+}) versus deficient (Sirt5^{-/-}) mice were used for all experiments.

(A–C) Relationship between mitochondrial (A) $\mathcal{J}O_2$, (B) mitochondrial $\Delta\psi_m$, and (C) NAD(P)H/NAD(P)⁺ redoxstate versus Gibbs energy of ATP hydrolysis (ΔG_{ATP}) in mitochondria energized with G/M, Pyr/M, Oct/M, and Succ/Rot.

(D) Mitochondria $\mathcal{J}O_2$ plotted against $\Delta\psi_m$ in the presence of G/M, Succ/R, and Oct/M.

(E) Calculated slopes from the linear portions of the data depicted in (A). Linear portions are located to the left of the dotted line on each graph.

(F) Mitochondria electron leak, expressed as a percentage ($J_{H_2O_2}/JO_2 \times 100 = \% \text{ electron leak}$), in the presence Pyr/M in Sirt5^{-/-} heart mitochondria compared to Sirt5^{+/+}.

(G) Quantified rates of ATP synthesis (J_{ATP}) in intact mitochondria energized with G/M, Pyr/M, Oct/M, and Succ/R; rates of NADH production (J_{NADH}) by various DH enzymes were measured in permeabilized mitochondria. Data are expressed as the percentage of MCD^{fl/fl} controls.

(H) Quantified CV activity.

(G and H) Data expressed as the percentage of fl/fl controls. Dotted red line represents 100% of Sirt5^{+/+} controls. Data are mean \pm SEM, n = 8/group and were analyzed by Student's t test. *p < 0.05. n represents biological replicates.

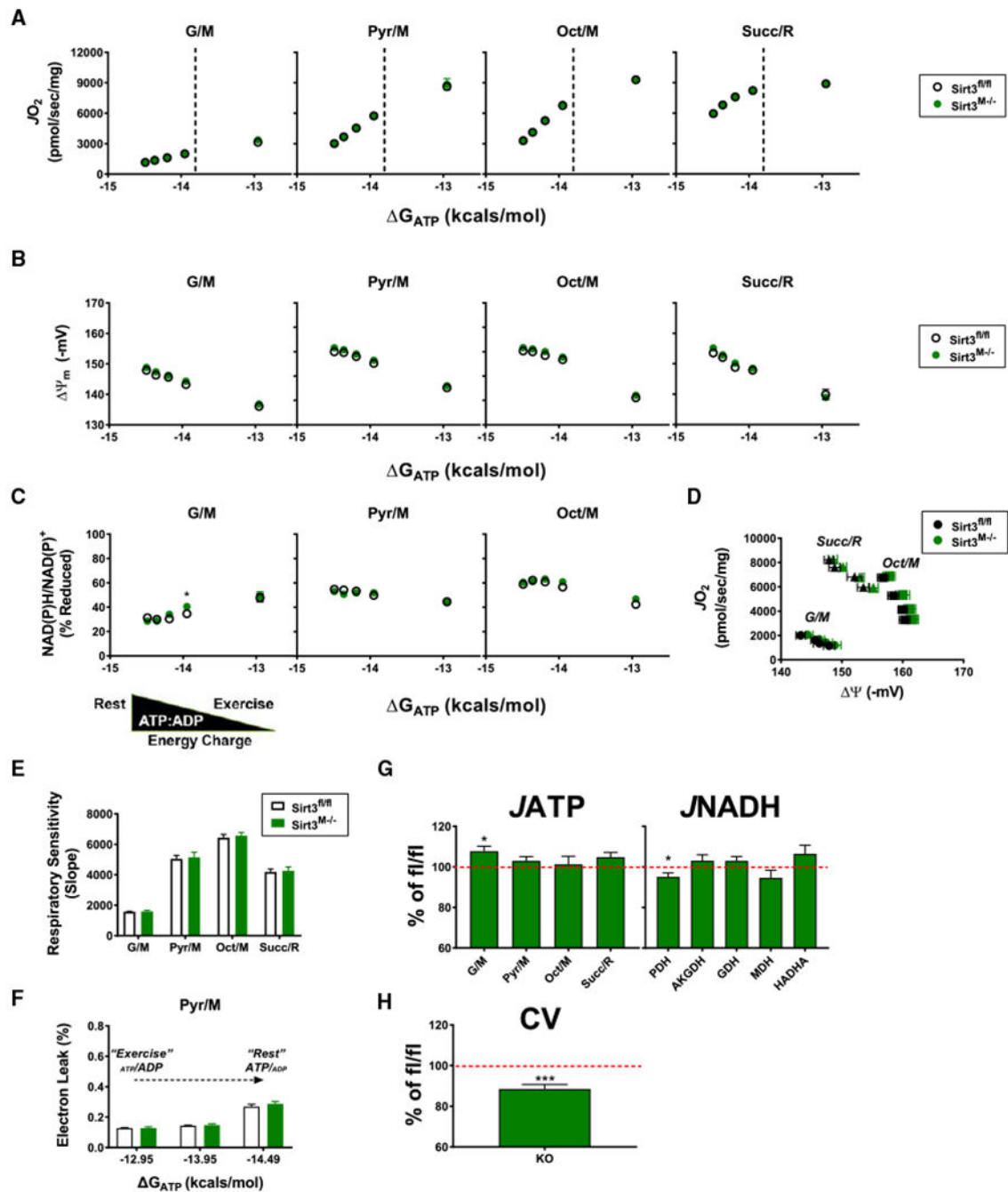


Figure 5. Comprehensive Assessment of Mitochondrial Energy Fluxes in the Setting of Sirt3 Deficiency

(A–H) Isolated mitochondria from hearts of Sirt3-competent (Sirt3^{fl/fl}) versus Sirt3-deficient (Sirt3^{M-/-}) mice were used for all experiments.

(A–C) Relationship between mitochondrial (A) $\mathcal{J}O_2$, (B) mitochondrial $\Delta\Psi$, and (C) NAD(P)H/NAD(P)⁺ redox state versus Gibbs’ energy of ATP hydrolysis (ΔG_{ATP}) in mitochondria energized with G/M, Pyr/M, Oct/M, and Succ/Rot.

(D) Mitochondria $\mathcal{J}O_2$ plotted against $\Delta\Psi$ in the presence of G/M, Succ/R, and Oct/M.

(E) Calculated slopes from the linear portions of the data depicted in (A). Linear portions are located to the left of the dotted line on each graph.

(F) Mitochondria electron leak, expressed as a percentage ($J_{H_2O_2}/JO_2 \times 100 = \% \text{ electron leak}$), in the presence Pyr/M in Sirt3-deficient heart mitochondria compared to WT.

(G) Quantified rates of ATP synthesis (J_{ATP}) in intact mitochondria energized with G/M, Pyr/M, Oct/M, and Succ/R; rates of NADH production (J_{NADH}) by various DH enzymes were measured in permeabilized mitochondria. Data are expressed as the percentage of MCD^{fl/fl} controls.

(H) Quantified CV activity.

(G and H) Data expressed as the percentage of fl/fl controls. Dotted red line represents 100% of fl/fl controls. Data are mean \pm SEM. n = 8/group and were analyzed by Student's t test.

*p < 0.05; **p < 0.001; ***p < 0.0001. n represents biological replicates.

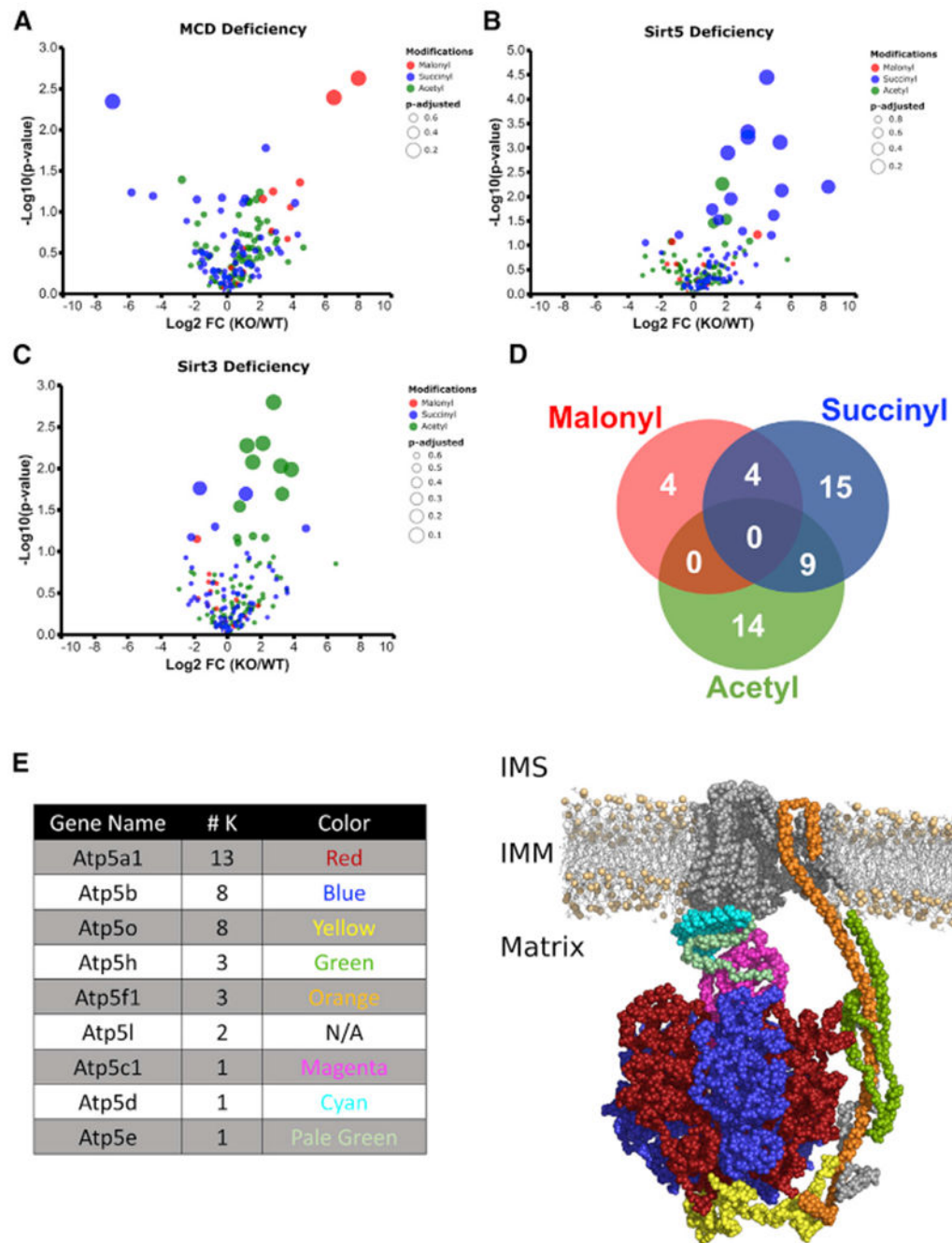


Figure 6. Comparisons of the CV Acylome across Multiple Loss-of-Function Models Reveals a Stochastic Pattern of Acylation

(A–C) Volcano plots depicting relative abundance of malonyl-peptides (red dots), succinyl-peptides (blue dots), and acetyl-peptides (green dots) identified within CV proteins isolated from hearts of mice with deficiency of (A) MCD, (B) Sirt5, or (C) Sirt3, expressed relative to fl/fl or +/+ controls.

(D) Overlapping acyl-peptides (color-coded for malonyl, succinyl, or acetyl) from each genetic model found to be elevated above controls ($> 1.5 \log_2 \text{FC}$).

(E) Graphical depiction of the identified lysine acylation events on CV across all three models. The color of each subunit is indicated in the table to the left. OMM, outer mitochondrial membrane; IMM, inner mitochondrial membrane. This figure was generated using the bovine crystal structure of ATP synthase (PDB: 5ARA) (Zhou et al., 2015).

Author Manuscript

Author Manuscript

Author Manuscript

Author Manuscript

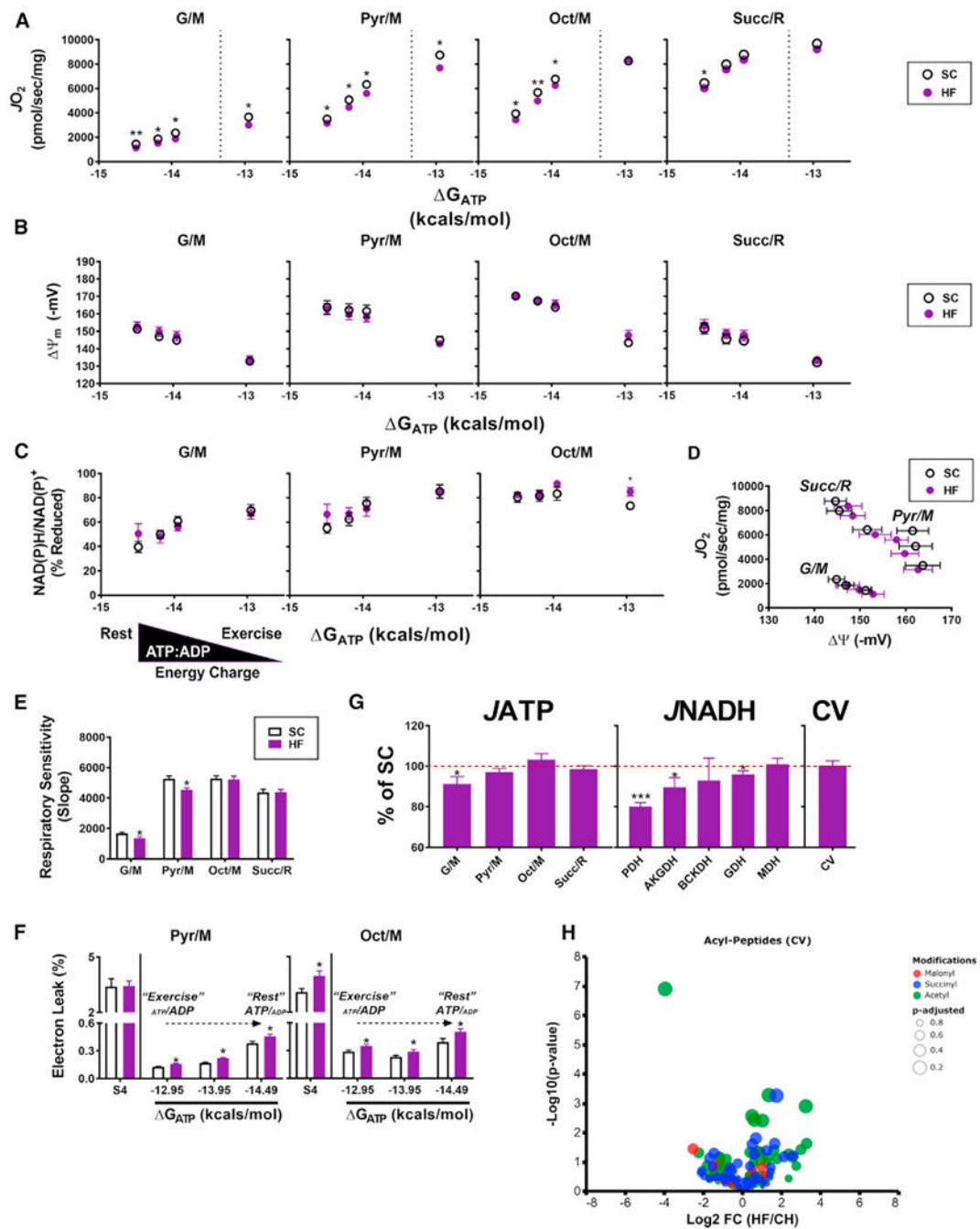


Figure 7. Comprehensive Assessment of Mitochondrial Energy Fluxes in the Setting of Overnutrition

(A–H) Isolated mitochondria from hearts of C57BL/6NJ mice fed a high-fat (HF) or standard chow (SC) diet were used for all experiments.

(A–C) Relationship between mitochondrial (A) $\dot{V}O_2$, (B) mitochondrial $\Delta\Psi_m$, and (C) NAD(P)H/NAD(P)⁺ redox state versus Gibbs' energy of ATP hydrolysis (ΔG_{ATP}) in mitochondria energized with G/M, Pyr/M, Oct/M, and Succ/Rot.

(D) Mitochondria $\dot{V}O_2$ plotted against $\Delta\Psi_m$ in the presence of G/M, Pyr/M, and Succ/R.

(E) Calculated slopes from the linear portions of the data depicted in (A). Linear portions are located to the left of the dotted line on each graph.

(F) Mitochondria electron leak, expressed as a percentage ($J_{H_2O_2}/JO_2 \times 100 = \% \text{ electron leak}$), in the presence Pyr/M and Oct/M.

(G) Quantified rates of ATP synthesis (J_{ATP}) in intact mitochondria energized with G/M, Pyr/M, Oct/M, and Succ/R; rates of NADH production (J_{NADH}) by various DH enzymes measured in permeabilized mitochondria, as well as CV activity. Data expressed as the percentage of SC controls. The dotted red line represents 100% of WT.

(H) Volcano plots depicting the relative abundance of malonyl-peptides (red dots), succinyl-peptides (blue dots), and acetyl-peptides (green dots) identified within CV proteins from HF mice relative to SC controls.

Data are mean \pm SEM. (A–G) $n = 11/\text{group}$ and (H) $n = 5/\text{group}$ and were analyzed by Student's t test. * $p < 0.05$; ** $p < 0.001$; *** $p < 0.0001$. n represents biological replicates.

KEY RESOURCES TABLE

REAGENT or RESOURCE	SOURCE	IDENTIFIER
Antibodies		
Total Rodent OXPHOS WB Antibody Cocktail	Abcam	Cat# ab1110413, RRID:AB_2629281
Malonyl-Lysine [Mal-K] MultiMab Rabbit mAb mix	Cell Signaling	Cat# 14942
ETFDH	Abcam	Cat# ab126576, RRID: AB_11141444
ETFA	Abcam	Cat# ab110316, RRID: AB_10865517
HADHA	Abcam	Cat# ab54477, RRID: AB_2263836
PDH E1 α	Abcam	Cat# ab110330, RRID: AB_10858459
Lipoic Acid	Millipore Sigma	Cat# 437695, RRID: AB_212120
Pan anti-malonyllysine antibody	PTM Biolabs	Cat# PTM-901, RRID: AB_2687947
MLYCD	Proteintech Group	Cat# 15265-1-AP, RRID: AB_2146403
Sirt5	Generous gift from Leonard Guarente (Massachusetts Institute of Technology, Cambridge, MA).	
PDH E1 α (pSer ²³²)	Millipore Sigma	Cat# AP1063
PDH E1 α (pSer ²⁹³)	Millipore Sigma	Cat# AP1062
Chemicals, Peptides, and Recombinant Proteins		
Tris salt of phosphocreatine	Millipore Sigma	Cat# P1937; CAS# 108321-17-1
Tris salt of ATP	Millipore Sigma	Cat# A9062; CAS# 102047-34-7
Potassium pyruvate	Combi-Blocks	Cat# QA-1116; CAS# 4151-33-1
Potassium NADP ⁺	Ark-Pharm, Inc	Cat# AK671068
Creatine kinase from rabbit muscle	Millipore Sigma	Cat# 10736988001
Amplex Ultra Red Reagent (AUR)	ThermoFisher Scientific	Cat# A36006
CellLytic M	Millipore Sigma	Cat# C2978
Tetramethylrhodamine methyl ester (TMRM)	ThermoFisher Scientific	Cat# T668
Phosphoenoyl-pyruvate	Millipore Sigma	Cat# 10108294001; CAS# 4265-07-0
Auranofin	Millipore Sigma	Cat# A6733;
Oligomycin	Millipore Sigma	Cat# 75351; CAS# 579-13-5
Rotenone	Millipore Sigma	Cat# R8875; CAS# 83-79-4
Potassium cyanide	Millipore Sigma	Cat# 60178; CAS# 151-50-8
Carbonyl cyanide 4-(trifluoromethoxy)phenylhydrazone (FCCP)	Millipore Sigma	Cat# C2920; CAS# 370-86-5
Peroxidase from horseradish (HRP)	Millipore Sigma	Cat# P8375; CAS# 9003-99-0
Superoxide dismutase (SOD)	Millipore Sigma	Cat# S9697; CAS# 9054-89-1
Glucose-6-phosphate Dehydrogenase (G6PDH)	Millipore Sigma	Cat# G6378; CAS# 9001-40-5
Malate dehydrogenase (MDH)	Millipore Sigma	Cat# 442610-M; CAS# 9001-64-3
Pyruvate Kinase/Lactic Dehydrogenase enzymes from rabbit muscle	Millipore Sigma	Cat# P0294
Hexokinase	Millipore Sigma	Cat# H4502; CAS#9002-07-7
Trypsin from porcine pancreas (Trypsin)	Millipore Sigma	Cat# T4799; CAS# 9001-51-8
Creatine Monohydrate	Millipore Sigma	Cat# C3630; CAS# 6020-87-7
Octanoyl-L-carnitine	Millipore Sigma	Cat# 50892; CAS# 25243-95-2
Malic acid (Malate)	Millipore Sigma	Cat# M1000; CAS# 97-67-6
Glutamic acid (Glutamate)	Millipore Sigma	Cat# G1501; CAS# 6382-01-0
Succinic acid (Succinate)	Millipore Sigma	Cat# S3674; CAS# 110-15-6
α -ketoglutaric acid (AKG)	Millipore Sigma	Cat# K1750; CAS# 328-50-7
3-Methyl-2-oxopentanoic acid (α -keto- β -methylvalerate)	Millipore Sigma	Cat# 198978; CAS# 3715-31-9
Isocitrate	Millipore Sigma	Cat# 58790; CAS# 20226-99-7

REAGENT or RESOURCE	SOURCE	IDENTIFIER
Adenosine diphosphate (ADP)	Millipore Sigma	Cat# A5285; CAS# 72696-48-1
Tetraphenylphosphonium (TPP ⁺)	Millipore Sigma	Cat# 218790; CAS# 2001-45-8
NADH	Millipore Sigma	Cat# N7004; CAS# 104809-32-7
Nicotinamide adenine dinucleotide (NAD ⁺)	Millipore Sigma	Cat# N1636; CAS# 53-84-9
L-Aspartic acid (Aspartate)	Millipore Sigma	Cat# A9256; CAS# 56-84-8
Acetoacetyl-CoA	Millipore Sigma	Cat# A1625; CAS# 1420-36-6
Coenzyme A	Millipore Sigma	Cat# C3019; CAS# 18439-24-2
Thiamine pyrophosphate	Millipore Sigma	Cat# C8754; CAS# 154-87-0
Pyridoxal 5'-phosphate	Millipore Sigma	Cat# P9255; CAS# 853645-22-4
1× cOmplete ULTRA mini EDTA-free protease inhibitor tablet	Roche	Cat# 5892791001
Nicotinamide	Sigma	Cat# N3376
iodoacetamide	Sigma	Cat# 11149-5G
DL-Dithiothreitol	Fluka	Cat# 43819-1G
Lysyl Endopeptidase, Mass Spectrometry Grade (Lys C)	Wako Chemicals	Cat# 125-05061
Sequencing-Grade Modified Trypsin	Promega	Cat# PAV5113
Sixplex Tandem Mass Tag (TMT) isobaric labeling kit	Thermo Fischer Scientific	Cat# 90061
Protein A/G agarose	Thermo Fischer Scientific	Cat# 20421
IAP buffer	Cell Signaling Technolgy	Cat# 9993
Native gel electrophoresis sample buffer	Thermo Fischer Scientific	Cat# BN2003
G-250 Coomassie sample additive	Thermo Fischer Scientific	Cat# BN2004
Experimental Models: Organisms/Strains		
C56BL/6NJ mice	The Jackson Laboratory	Stock# 005304
Data and Software Availability		
Jupyter notebook containing the adjustment calculations interspersed with procedural descriptions needed to calculate GATP.	N/A	https://github.com/dmpio/bioenergetic-calculators/blob/master/jupyter_notebook/creatine-kinase-clamp.ipynb
Web-based GATP calculator	N/A	https://dmpio.github.io/bioenergetic-calculators/ck_clamp/
Proteome Discoverer 2.2	Thermo Fisher Scientific	Cat# IQLAAEGABSAFKJMAUH
Raw LC-MS/MS proteomics data	Proteome Xchange jPOST	Accession PXD011375 Accession JPST000507
Other		
QuantaMaster Spectrofluorometer	Horiba Scientific	Cat# QM-400
Glass screw neck autosampler vials	Waters	Cat# 600000671cv
4-16% BisTris Native gel	Thermo Fischer Scientific	Cat# BN1004
C18 ZipTips	Millipore	Cat# ZTC18S096
μC18 SEP-PAK Solid Phase Extraction columns (50 mg and 100mg)	Waters	Cat# WAT054960 Cat# WAT036820
Pierce high pH Reversed-Phase Peptide Fractionation Kit	Thermo Fischer Scientific	Cat# 84868
Pierce Quantitative Colorimetric Peptide Assay	Thermo Fischer Scientific	Cat# 23275
Pierce BCA Protein Assay Kit	Thermo Fischer Scientific	Cat# 23225